Bioorganic Chemistry 174 (2026) 109740

Contents lists available at ScienceDirect

Bioorganic Chemistry

journal homepage: www.elsevier.com/locate/bioorg

Synthesis and cytotoxic evaluation of pyrido-dipyrimidine derivatives: Mechanism of action, DNA and HSA binding studies

Lazar Milović [a], Nađa Grozdanić [b], Tatjana Stanojković [b], Jelena Đorović Jovanović [a], Svetlana Jeremić [c], Maja Petrović [b], Milica Marković [d], Ana Rilak Simović [a], Nenad Janković [a,*]

[a] University of Kragujevac, Institute for Information Technologies Kragujevac, Department of Science, Liceja Kneževine Srbije 1A, 34 000 Kragujevac, Serbia
[b] Institute for Oncology and Radiology of Serbia, Pasterova 14, 11 000 Belgrade, Serbia
[c] State University of Novi Pazar, Department of Natural and Mathematical Sciences, Vuka Karadžića 9, 36300 Novi Pazar, Serbia
[d] University of Belgrade, Faculty of Pharmacy, Vojvode Stepe 450, 11221 Belgrade, Serbia

ARTICLE INFO

Keywords:
Pyrido-dipyrimidines
Cytotoxicity
DNA binding
HSA interaction
Molecular docking

ABSTRACT

This study presents the synthesis of a novel series of pyrido[2,3-d:6,5-d']dipyrimidine derivatives (**4a-v**) *via* an 'on-water' multicomponent reaction, utilizing thiobarbituric acid, diverse aldehydes, and amines at room temperature. The compounds were evaluated for cytotoxic activity against human cancer cell lines (HeLa, K562, LS174, A549) and normal fibroblasts (MRC-5) using MTT assays. Notable potency was observed against HeLa and K562 cells, with IC_{50} values ranging from 9.82 to 192.47 μM. Compound **4k** exhibited the strongest activity against HeLa ($IC_{50} = 9.82 \pm 1.07$ μM) with a selectivity index (SI) >12, while **4u** was most effective against K562 ($IC_{50} = 17.36 \pm 1.39$ μM, SI >9). LS174 and A549 showed limited sensitivity. Structure-activity relationship (SAR) analysis revealed that *para*-hydroxyphenyl substituents at position 5 and thiocarbonyl groups enhanced cytotoxicity, particularly against leukemia cells, *via* improved hydrogen bonding and target affinity. Mechanistic studies on **4k** and **4u** focused on DNA and human serum albumin (HSA) interactions. UV–Vis and fluorescence spectroscopy, including ethidium bromide displacement and viscosity measurements, indicated minor groove binding to CT-DNA ($K_b \sim 10^4\ M^{-1}$; $K_{sv} \sim 10^4\ M^{-1}$) with partial intercalation. HSA binding occurred *via* static quenching at sites I and II ($K_{sv} \sim 10^5\ M^{-1}$; $K_b \sim 10^5\ M^{-1}$), confirmed by competitive assays with Eosin Y and ibuprofen. Cell cycle analysis and AO/EB staining demonstrated apoptosis induction, with increased subG1 populations. Caspase assays showed **4k** activated both intrinsic (caspase-9) and extrinsic (caspase-8) pathways in HeLa cells, leading to caspase-3 execution; **4u** induced caspase-independent apoptosis in K562. Molecular docking and dynamics simulations supported minor groove DNA preference and HSA site I/II binding, with stable complexes ($\Delta G_{bind} \leq -8$ kcal/mol). RMSD, RMSF, and Rg analyses affirmed structural integrity. These derivatives emerge as promising selective anticancer agents targeting DNA and apoptosis, warranting further optimization and *in vivo* studies.

1. Introduction

Heterocyclic compounds, particularly nitrogen-containing heterocycles, have widely been presented in pharmacological agents. Pyridines and pyrimidines are separately investigated and evaluated compounds with different uses and condensed polycyclic scaffolds having both of those molecules have been studied recently. Progress in synthesis of these molecules has been achieved by usage of combinatory chemistry and multicomponent reactions (MCR) [1]. This approach reduces steps in process of synthesis, which is more sustainable way and in accordance with green chemistry principles [2]. Some methods of making this class of compounds are Michael addition of amino aldehyde to 1,3-diarylbarbituric acid [3], condensation reaction which involves 6-amino uracil, urea and aromatic aldehyde catalyzed by HOAc [4], one-pot green synthesis from uracil derivatives, using nanocatalyst [5] or microwave inducted reaction between uracil derivatives and aromatic aldehydes [6].

Pyridopyrimidines, as the fused heterocyclic compounds, are already known as potential agent for various biological activities. Biological activities that these molecules have manifested are: anticancer, proved

* Corresponding author.
E-mail address: nenad.jankovic@uni.kg.ac.rs (N. Janković).

https://doi.org/10.1016/j.bioorg.2026.109740
Received 10 December 2025; Received in revised form 21 February 2026; Accepted 8 March 2026
Available online 12 March 2026

forming of oligonucleosomal fragments in solution after treating with DNA [7]; antimicrobial against Gram negative bacteria, yeast and fungi [8]; antioxidant, where results from DPPH assay were low in relation to ascorbic acid and quercetin, but near the activity value of dihydropyridines [9]; anti-inflammatory, based on inhibition of colony growth factor receptor [10]; anti-proliferative [11]; *etc.* Similar activities of pyrido-dipyrimidines (PDP) have not been investigated enough, although they showed some in published papers [12] such as anticancer [13], antimicorbal [14], analgesic and anti-inflamatory activites [15]. Insufficient examination inspired us to research this area of application of pyrido-dipyrimidines.

Aldehydes used in presented work were mostly vanillin derivatives. Vanillin itself has been examined because of anticancer [16,17] and mainly antioxidant [18,19] properties, and widely used at mass production in food industry [20–22].

Design of the compounds, which are able to bind with DNA, is a very important part in cancer research. Anticancer activity of many compounds is based on their binding with DNA, resulting in actions of changing DNA replication and stoppage of tumor growth [23]. Chemotherapeutics, working this way, have shown real effectiveness and less toxicity, compared to other pharmaceutics [24], and that is reason for synthesis number of compounds with therapeutic potential. Pyrimidine cycles containing structures also have ability to intercalate between DNA chains, regarding this, pyrimidine derives showed apoptotic effect toward DNA [25]. Organic heterocyclic compounds, not coordinated with metals, are inhibitors for topoisomerase I and II enzymes, which can stop DNA replication without cytotoxicity [26,27]. The cytotoxicity of most metal free heterocyclic-based drugs are based on their ability to suppress topoisomerase activity hence the topoisomerase acts as an endogenous poison and may induce apoptosis.

The aim of this study was to synthesize a series of pyrido[2,3-*d*:6,5-*d'*]dipyrimidine derivatives under 'on water' conditions, evaluation of their cytotoxic activity against selected cancer cell lines, and investigation of the interaction with DNA and human serum albumin through spectroscopic and computational methods for the most active ones.

2. Methods and materials

2.1. General information

All substrates, including vanillin (99.5%), thiobarbituric acid (99%), amines, calf thymus DNA (CT-DNA), ethidium bromide (EB), human serum albumin (HSA), Eosin Y, ibuprofen, phosphate buffer (PBS, 10 mM, $C_{NaCl} = 137$ mM, $C_{KCl} = 2.7$ mM, pH = 7.4) were purchased from Sigma Aldrich. Melting points (Mp) were measured using a Mel–Temp apparatus and are reported without correction. IR spectra were recorded on a Perkin–Elmer Spectrum 3 FT-IR/FIR spectrometer. The UV–Vis spectra were recorded on a PerkinElmer Lambda 35 double beam spectrophotometer, using 1.0 cm path-length quartz cuvettes (3.0 mL). Fluorescence measurements were carried out on an RF-1501 PC spectrofluorometer (Shimadzu, Japan). Anton Paar rolling-ball viscometer with Lovis 2000 M/ME (Anton Paar GmbH) was used for measurements. The excitation and emission bandwidth were both 10 nm. Compounds **4a-v** were characterized using a Varian Gemini 200 MHz NMR spectrometer (^{1}H at 200 and ^{13}C at 50 MHz) at 288 K in DMSO-d_6 solution. All spectra are given in Electronic Supplementary Materials (ESI, Figs. S1-S44). The purity of selected compounds was checked using a C18 column (4.6 × 100 mm, 3.5 μm) on a Perkin Elmer Flexar HPLC system with UV/Vis detection and autosampler at flow rate 0.7 mL/min (Fig. S54), mobile phase with acetonitrile/water mixture.

2.2. General procedure of synthesis 4a-v

In a 25 mL round-bottom flask 10 mL of water, thiobarbituric acid **1** (1 eq, 0.5 mmol, 0.072 g), and aldehyde **2** (1 eq, 0.5 mmol) were added. After 1.5 h, an additional equivalent of thiobarbituric acid and amine **3** (1 eq, 0.5 mmol) were added to the reaction mixture. The mixture was stirred at room temperature, and the reaction progress was monitored by TLC using EtOAc: hexane as the eluent. The reaction was completed within 12–48 h, during which the desired product precipitated as a solid. The precipitate was collected by vacuum filtration, washed thoroughly with 70% aqueous ethanol (3 × 10 mL) to remove unreacted starting materials, and dried under reduced pressure.

2.3. DNA/HSA binding mode

2.3.1. UV–Vis Absorption method

The binding interactions of compounds **4k** and **4u** with CT-DNA were investigated using UV–Vis spectroscopy. Experiments were conducted at 25 °C in a 10 mM PBS buffer (pH 7.4). Absorption titration was carried out by maintaining a constant compound concentration (1 mM) and incrementally adding DNA stock solution until a 1:10 ratio (2.6 mM DNA) was achieved.

2.3.2. Fluorescence quenching measurements

2.3.2.1. DNA binding studies. The competitive interactions between EB and the compounds **4k** and **4u** in the presence of CT-DNA were examined using fluorescence spectroscopy. Measurements of fluorescence intensity were carried out with an excitation wavelength of 527 nm and an emission wavelength of 612 nm. Stock solutions were prepared as follows: DNA at 2.6 mM, and both compounds at 1 mM, all dissolved in 10 mM PBS at pH 7.4. DNA-compound mixtures were made by combining the DNA stock with various concentrations of the test compounds. For the fluorescence experiments, the final DNA concentration was kept constant at 29.5 μM, while the concentrations of the compounds ranged from 2.95 to 29.5 μM. Before recording the measurements, each sample was mixed thoroughly and incubated at room temperature for 5 min. The emission spectra were collected across a wavelength range of 550 to 750 nm.

2.3.2.2. Albumin binding assays. To investigate the interactions between human serum albumin (HSA) and the compounds **4k** and **4u**, fluorescence quenching experiments were conducted. These experiments rely on monitoring the natural fluorescence of tryptophan residues in HSA as they interact with the test compounds. A 2 μM HSA solution was prepared in 10 mM PBS at pH 7.4, while the compounds were prepared at a concentration of 1 μM. Increasing amounts of compound **4k** were added to the HSA solution up to a final concentration of 7×10^{-6} M, while compound **4u** was added up to a concentration of 5×10^{-6} M. Fluorescence spectra were recorded between 300 and 500 nm, using an excitation wavelength of 285 nm and monitoring emission at 358 nm. Control experiments confirmed that the compounds alone did not fluoresce under these conditions. The strengths of the interactions between HSA and the test compounds were evaluated using Stern–Volmer and Scatchard analyses to determine binding constants. Furthermore, competitive binding studies were performed using eosin Y (site I marker) and ibuprofen (site II marker) to examine the affinity of compounds **4k** and **4u** for specific HSA binding sites. For these experiments, HSA and the site markers were mixed at equal concentrations (2.0×10^{-6} M), and the compounds were titrated with increasing amounts of eosin Y (up to 5.0×10^{-6} M) or ibuprofen (up to 2.0×10^{-6} M for **4k** and 9.0×10^{-6} M for **4u**). Fluorescence measurements were performed with excitation at 295 nm and emission recorded from 300 to 500 nm.

2.3.3. Viscosity

Viscosity measurements were conducted using Anton Paar rolling ball viscometer with Lovis 2000 M/ME (Anton Paar GmbH) at 25 °C. Series of samples with constant DNA concentration (2.6 mM) and varying compounds concentrations (2–20 μM) for final molar ratios (0,

0.1, 0.2, 0.3, 0.4, 0.5, 0.6, 0.7, 0.8, 0.9, and 1.0) were prepared. The viscosity of the DNA solution was recorded as η_0, while **4k-** or **4u**-CT-DNA samples viscosity was recorded as η. Plotting the values of the cube root of relative specific viscosity, or $(\eta/\eta_0)^{1/3}$, against the r = [compound]/[DNA] was done.

2.4. Cell culture

Cervical adenocarcinoma cell line (HeLa), chronic myelogenous leukemia cell line (K562), human colon carcinoma cell line (LS174T), non-small cell lung carcinoma cell line (A549), and a normal human fetal lung fibroblast cell line (MRC-5) were maintained in RPMI-1640 medium contained 10% fetal bovine serum (FBS), L-glutamine, and penicillin-streptomycin (Sigma). Cells were incubated in a humidified atmosphere of 95% air and 5% CO_2 at 37 °C. The cell lines were acquired from the American Type Culture Collection (Manassas, VA, USA).

2.5. Reagents for cell culture experiments

Unless otherwise indicated, all chemicals used in the cell culture experiments were purchased from Sigma Aldrich (MA, USA). Cell culture procedures were carried out using Thermo Scientific™ Biolite™ 96-well and 6-well plates, as well as 25 cm^2 flasks, unless specified otherwise.

2.6. In vitro cytotoxic activity

The cytotoxic activity of 25 compounds was determined against four human malignant cell lines: HeLa, K562, LS174, A549, as well as against normal human MRC-5 cell line. The cells were seeded into 96-well microtiter plates: HeLa (2,000 cells per well), K562 (5,000 cells per well), LS174 (7,000 cells per well), A549 (5,000 cells per well) and MRC-5 (5,000 cells per well). The compounds were dissolved in dimethyl sulfoxide at concentration of 10 mM and the cells were treated with five concentrations of compounds (12.5, 25, 50, 100, and 200 μM) after 24 h of cell adhesion. Following a 72 h incubation period, 10 μL of MTT [3-(4,5-dimethylthiazol-2-yl)-2,5-dyphenyl tetrazolium bromide] solution (5 mg/mL) was added to each well of the 96-well microtiter plates. This was followed by the addition of 100 μL of 10% sodium dodecyl sulfate (SDS) after 4 h. The absorbance was read at 570 nm using a Thermo Scientific™ Multiskan SkyHigh microplate spectrophotometer. Two independent experiments were performed in triplicate and the IC_{50} value is defined as the concentration of an agent that inhibits cell survival by 50%, compared to the control cells. The selectivity index was calculated by dividing the IC_{50} value obtained for the normal MRC-5 cell line by the IC_{50} value determined for the corresponding malignant cell line. The used MTT protocol was firstly established by Mosmann [28], modified by Ohno and Abe [29], and described by Matić et al. [30].

2.7. Cell cycle analysis

The cells were seeded in six-well plate: 200,000 HeLa and 250,000 K562 cells per well. After 24 h, HeLa cells were treated with compound **4k**, while K562 were treated with compound **4u**. The concentrations used corresponded to IC_{50} and 2 × IC_{50} values, which were calculated based on cell viability at 24 and 48 h after treatment. Control cells were grown in cell culture medium only. Following a 24 h and 48 h incubation, the cells were collected and fixed in cold 70% ethanol on ice. The cells were stored at −20 °C for at least one week. After fixation, the samples were washed and treated with RNase (100 μg/mL) at 37 °C temperature. Following 30 min incubation period, the solution of propidium iodide (PI) (40 μg/mL) was added and the cells were incubated for 10 min before analysis. Cell-cycle distribution was analyzed using a BD FACSCalibur™ flow cytometer (BD Biosciences). Data analysis was performed using BD CellQuest™ Pro software on a minimum of 10,000 cells per sample.

2.8. Fluorescence microscopy for apoptosis assessment

HeLa cells were seeded into 6-well plates on the coverslips (50,000 cells per well) in complete RPMI-1640 medium. The HeLa cells were cultured for 24 h at 37 °C in a humidified atmosphere containing 5% CO_2 to allow for adherence. K562 cells were seeded and incubated for 2 h in the same conditions. Following initial incubation, the cells were treated for 48 h with the **4k** (HeLa) and **4u** (K562) compounds (IC_{50} and 2 × IC_{50} concentrations). Post-treatment, cells on the coverslips were stained with a mixture of two dyes [3 μg/mL acridine orange and 10 μg/mL ethidium bromide in phosphate-buffered saline (PBS)]. K562 cells as well as supernatant of Hela cells were collected and centrifuged at 2000 RPMI for 5 min, and then stained with 15 μL of the dye mixture. Photomicrographs were acquired using a Carl Zeiss PALM Microbeam AxioObserver. Z1 fluorescence microscope equipped with an AxioCam MRm camera, utilizing Alexa 488 (for AO) and Alexa 568 (for EB) filter sets.

2.9. Measurement of Intracellular ROS Production

Intracellular ROS levels were evaluated by flow cytometry using 2′,7′-dichlorofluorescin diacetate (DCFH-DA). Cells (200,000/well) were treated with compounds **4k** or **4u** at IC_{20} concentrations for 24 h. Hydrogen peroxide (H_2O_2 (100 μM) was added to the control cells 30 min prior to analysis to serve as a positive control. Following treatment, cells were incubated with 20 μM DCFH-DA for 30 min at 37 °C in the dark. Green fluorescence (DCF) was measured using a BD FACSCalibur flow cytometer (FL1 channel). A total of 15,000 events were recorded for each sample. Data acquisition and analysis were performed using CellQuest Pro software (BD Biosciences). The experiment was performed in triplicate, and results are expressed as the fold change of the fluorescence intensity geometric mean (Geo Mean) relative to the untreated control.

2.10. Caspase inhibition assay

To test caspases involved in the apoptotic pathway induced by compounds **4k** and **4u**, a caspase inhibition assay was performed. 200,000 HeLa cells per well were seeded in six-well plate and incubated for 24 h, as well as, 250,000 K562 cells per well and incubated for 2 h at 37 °C in a humidified atmosphere containing 5% CO_2. Then both HeLa and K562 cells were incubated for 2 h with specific inhibitors for caspase-3 (Z-DEVD-FMK), caspase-8 (Z-IETD-FMK), and caspase-9 (Z-LEHD-FMK) at a final concentration of 40 μM. Following pre-incubation, cells were treated for 24 h with compounds **4k** (HeLa) and **4u** (K562) at their respective 2 × IC_{50} concentrations. Control groups consisted of cells treated with the compounds alone, without prior exposure to caspase inhibitors. After treatment, the cells were harvested by centrifugation, washed with PBS, and fixed in ice-cold 70% ethanol. The samples were stored at −20 °C for up to 7 days. For cell cycle analysis, fixed cells were stained with a propidium iodide (PI) solution. The percentage of cells in the subG1 phase (indicative of apoptosis) was quantified using flow cytometry.

2.11. Molecular docking simulation

In order to examine the possibility of inhibition of DNA molecules by the molecules **4u** and **4k** examined here, the molecular docking analysis was applied. For this purpose, the DNA molecule sequence taken from the PDB database (PDB ID: 1M6F) was used as a target molecule [31]. The possibility of inhibition of HSA molecules was examined by the same method. For this purpose, HSA, whose structure was also taken from the PDB database (PDB ID: 7DJN), was used as a target molecule [32]. Preparation of target molecules for use in molecular docking analysis, which involved the removal of water molecules, as well as the removal of appropriate ligands, was performed using the BIOVIA

Discovery Studio [33]. The molecular docking analysis is performed using AutoDock 4.2 and AMDock software packages [34,35]. To analyze the entire DNA molecule during molecular docking, a gridbox of dimensions 60 × 60 × 120 npts is used, while the gridcenter was positioned at the coordinates 8.796 14.255 Å × 20.566 Å × 8.796 Å in relation to the *x*, *y* and *z* axes. Bearing in mind that the HSA molecule is significantly larger than the DNA molecule, and to rationalize the time required for the analysis, the position of the active site of the protein and the dimensions of the corresponding gridbox were determined for this molecule using the AGFR software [36]. Thus, the dimensions of the gridbox for molecular docking analysis involving HSA were set to 64 × 54 × 54 npts, and the grid center was positioned at 15.002 Å × 23.113 Å × 20.023 Å relative to the *x*, *y*, and *z* axes of the coordination system. Both mentioned grid boxes possess a point spacing of 0.375 Å.

During receptor-ligand docking, for which a Lamarckian genetic algorithm was applied [37], the target structure was considered rigid, while the ligand structure was flexible. Ligand molecules were previously prepared for docking analysis by geometry optimization. Ligand geometry was performed using the M06-2X/6-311++G(d,p) level of theory implemented in the Gaussian 09 program package [38]. Bearing in mind that the investigated molecules **4u** and **4k** have acidic hydrogen atoms, the percentage concentration of the active species of the considered molecules at pH = 7.4 was determined using the Playground server [39]. The optimization of the geometry of the ionic species, which are assumed to be formed in significant concentration under physiological conditions by the deprotonation of neutral molecules, was performed using the same level of theory as the corresponding neutral forms. The identified ionic species were also considered as potential ligands in the molecular docking analysis.

2.12. Molecular dynamics simulation

For the investigation of the structural stability and interaction profiles of the protein–ligand complexes obtained from molecular docking simulations, molecular dynamics (MD) simulations were carried out using the AMBER24 software package [40,41]. Initial conformations for the MD runs were selected from the docking results, prioritising the most stable complexes based on the lowest calculated free binding energies. Each system was solvated in an explicit water environment employing the TIP3P water model [42]. The ionic concentration was adjusted by adding Na^+ and Cl^- ions to ensure overall electroneutrality. Ligand parameters were generated using the RESP (Restrained ElectroStatic Potential) method for partial charge derivation and the General AMBER Force Field (GAFF) for topology assignments. The protein was parameterised with the ff14SB force field [43,44], optimized for biomolecular simulations. The prepared systems were first subjected to energy minimisation under the NVT ensemble to remove steric clashes and relax the structure, followed by equilibration under the same ensemble conditions. Production of MD simulations was performed for 50 ns with an integration time step of 2 fs, employing the SHAKE algorithm to constrain covalent bonds involving hydrogen atoms. The production stage utilized the NPT ensemble to maintain constant pressure and temperature. All production simulations were performed using the CUDA-enabled pmemd engine in AMBER24, which enables efficient GPU-accelerated computation [41,45]. Periodic boundary conditions were applied throughout, and long-range electrostatic interactions were computed using the Particle Mesh Ewald (PME) method [46]. For nonbonded interactions, a 10 Å cutoff was applied.

3. Results and discussion

3.1. Synthesis of 4a-v

Pyrido-dipyrimidines (**4a-v**) were synthesized using an eco-friendly method. Different amines and aldehydes, mostly vanillin based, have been used to obtain a variety of products. Reaction was performed in water at room temperature providing desired products in good yields (Scheme 1).

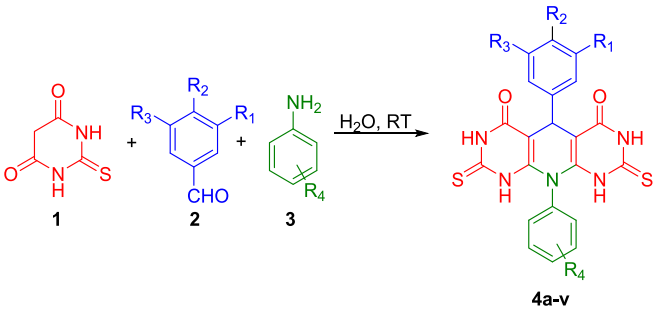

Scheme 1. General synthetic outline of **4a-v**.

Table 1
Structures of 4a-v.

Compound	R_1	R_2	R_3	R_4
4a	–H	$–OCH_2Ph$	–H	–H
4b	$–OCH_3$	$–OCH_2Ph$	–H	–H
4c	$–OCH_3$	–OH	–Br	–H
4d	$–OCH_3$	$–OCH_2Ph$	–H	*p*-CH_3
4e	$–OCH_3$	$–OCH_2Ph$	–H	*m*-OCH_3
4f	$–OCH_3$	$–OCH_2Ph$	–H	*p*-Cl
4g	$–OCH_3$	–OAc	–H	*p*-CH_3
4h	$–OCH_3$	–OAc	–H	*p*-OH
4i	$–OCH_3$	–OAc	$–NO_2$	*p*-OH
4j	$–OCH_3$	Decyloxy	–H	*p*-Cl
4k	$–OCH_3$	Hexyloxy	–H	*p*-OH
4l	$–OCH_3$	–OH	–I	*p*-Cl
4m	$–OCH_3$	–OH	–I	*p*-OCH_3
4n	$–OCH_3$	–OH	$–NO_2$	*p*-CH_3
4o	$–OCH_3$	–OH	$–NO_2$	*o*-OH
4p	$–OCH_3$	–OH	$–NO_2$	*p*-OH
4q	$–OCH_3$	–OH	$–NO_2$	*m*-OCH_3
4r	$–OCH_3$	–OH	$–NO_2$	*p*-Cl
4s	$–OCH_3$	–OH	$–NO_2$	*p*-Br
4t	$–OCH_3$	–OCOPh	$–NO_2$	*p*-Br
4u	$–OCH_3$	–OH	–Br	*p*-OH
4v	$–OCH_3$	–OH	–I	*p*-OH

The Table 1 presents a series of substituents attached at aldehyde and amine molecular scaffold. Each compound is defined by four variable substituents (R_1, R_2, R_3, R_4).

3.2. DNA/HSA binding mode

3.2.1. UV–Vis spectrophotometry

Interactions between DNA and compounds can occur through various mechanisms, such as covalent bonding, minor or major groove binding, intercalation, or electrostatic interactions. UV–Vis absorption spectroscopy is used to evaluate the overall DNA binding affinity. The binding strength of these compounds, **4k** and **4u,** was determined by monitoring spectral changes as the concentration of CT–DNA increased (see Figs. S45 and S46**,** ESI). An increase in molar absorptivity of the absorption bands (hyperchromic shifts) was observed, confirming binding interactions (Figs. S45 and S46). The binding constants (K_b) were calculated using equation (Eq 1):

$$[\mathrm{DNA}]/(\varepsilon_A-\varepsilon_f) = [\mathrm{DNA}]/(\varepsilon_b-\varepsilon_f) + 1/[K_b(\varepsilon_b-\varepsilon_f)] \quad (1)$$

where [DNA] represents the DNA concentration in base pairs, $\varepsilon_A = A_{obsd}/[\mathrm{compound}]$ is the apparent extinction coefficient, ε_f is the extinction coefficient of the free compound and ε_b is the extinction coefficient of the fully bound compound.

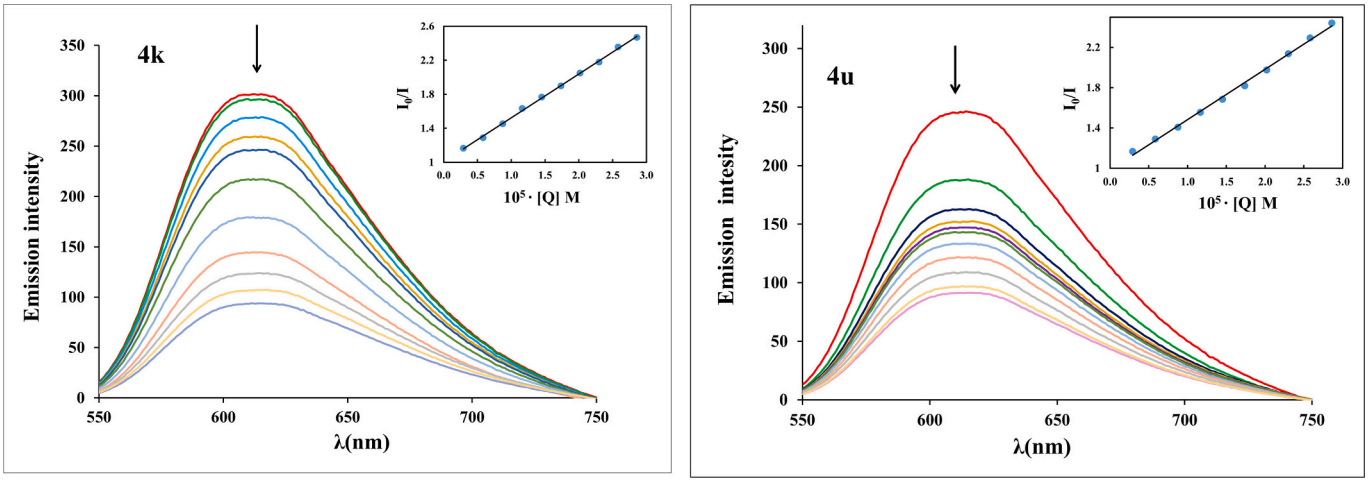

Fig. 1. Fluorescence spectra of EB-CT DNA in the absence (red lines) and the presence of varying amounts of compounds **4k** and **4u**. Insert graphs: Stern–Volmer plots of EB-CT DNA for compounds **4k** and **4u**. (For interpretation of the references to colour in this figure legend, the reader is referred to the web version of this article.)

Table 2
The DNA-binding constants (K_b) and Stern–Volmer constants (K_{sv}) for **4 k** and **4u** from EB-DNK.

Compound	K_b [M^{-1}]	K_{sv} [M^{-1}]
4k	$(2.06 \pm 0.1) \times 10^3$	$(5.24 \pm 0.4) \times 10^4$
4u	$(6.37 \pm 0.3) \times 10^3$	$(4.61 \pm 0.1) \times 10^4$

3.2.2. *Fluorescence quenching measurements*

3.2.2.1. DNA-binding studies. The binding interactions between compounds **4k** and **4u** and CT-DNA were examined using EB displacement assays. In aqueous solution, EB exhibits weak fluorescence; however, its fluorescence intensity increases markedly upon intercalation between DNA base pairs, emitting strongly around 600 nm. When either **4k** or **4u** was introduced into the pre-formed EB–CT-DNA complex, a significant decrease in fluorescence was observed, indicating that the compounds effectively displaced EB from the DNA helix.

To quantify these interactions, fluorescence quenching data were analyzed using the Stern–Volmer equation (**Eq. 2**):

$$I_0/I = 1 + k_q\,\tau_0\,[Q] = 1 + K_{SV}[Q] I_0/I = 1 + k_q\tau_0[Q] = 1 + K_{SV}[Q] \qquad (2)$$

Where τ_0 is the fluorescence lifetime of the emitter in the absence of a quencher, and k_q is the bimolecular quenching constant, I_0 and I are the fluorescence intensity in the absence and presence of a quencheris, and [Q] is concentration of quencher.

EB displacement experiments were conducted by gradually increasing the concentration of the compounds and recording the corresponding changes in fluorescence emission of the EB–DNA complex. Both **4k** and **4u** induced a concentration-dependent quenching of EB fluorescence.

The Stern–Volmer quenching constants (K_{sv}) were derived from the respective plots (Fig. 1), and the results are summarized in Table 2. The obtained K_{sv} values were similar to those reported for known minor groove-binding agents [47], suggesting that **4k** and **4u** likely interact with CT-DNA *via* minor groove binding rather than classical intercalation.

3.2.2.2. HSA binding studies. The pharmacological behavior of a drug is significantly influenced by its distribution between its free and protein-bound forms in the bloodstream. In particular, the extent of a drug's interaction with major plasma proteins, such as human serum albumin (HSA), plays a crucial role in modulating its bioavailability and therapeutic efficacy. Binding to HSA is especially advantageous for targeted drug delivery, as it can facilitate the selective accumulation of

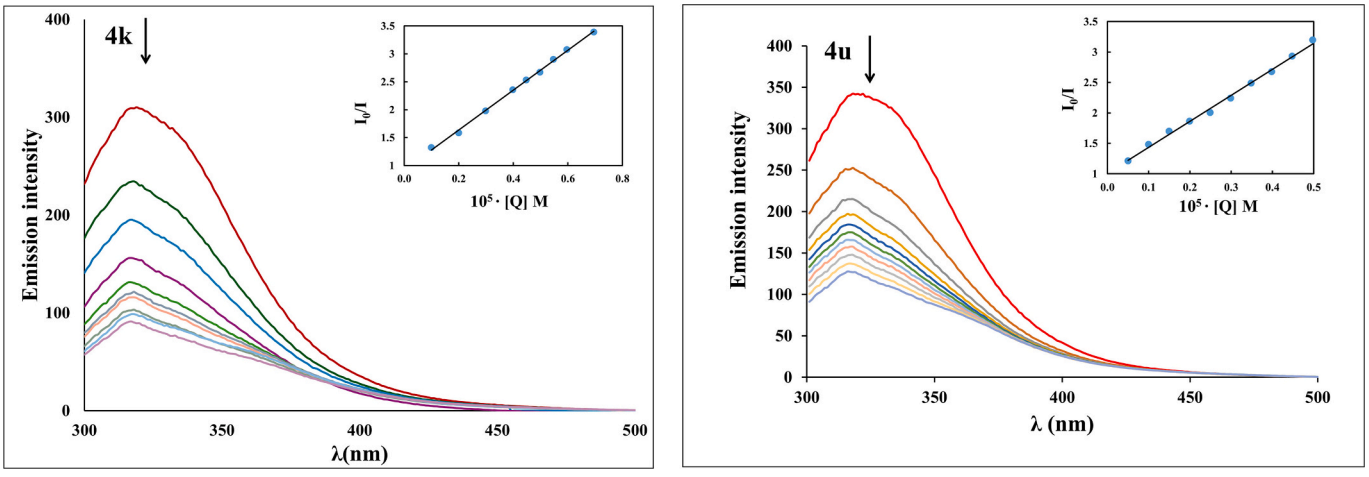

Fig. 2. Fluorescence spectra of HSA in the absence (red lines) and presence of varying amounts of compounds **4k** and **4u**. Insert graphs: Stern–Volmer plots of HSA for compounds **4k** and **4u**. (For interpretation of the references to colour in this figure legend, the reader is referred to the web version of this article.)

Table 3
Stern-Volmer constants (K_{sv}) and bimolecular quenching constans (k_q), binding constant (K_b) and number of the binding sites (n) for the interaction of compounds **4k** and **4u** with HSA, and site markers Eosin Y and Ibuprofen.

Compound	*Compound-HSA*	*Compound-HSA-Eozin Y*	*Compound-HSA-Ibu*
		K_{sv} [10^5 M^{-1}]	
4k	4.49 ± 0.20	2.56 ± 0.40	4.50 ± 0.40
4u	4.23 ± 0.10	2.71 ± 0.20	3.05 ± 0.10
		k_q [10^{13} M^{-1} s^{-1}]	
4k	4.49	2.56	4.50
4u	4.23	2.71	3.05
		K_b	
4k	8.59 ± 0.20	0.76 ± 0.40	1.38 ± 0.40
4u	2.56 ± 0.10	1.08 ± 0.20	7.78 ± 0.10
		n	
4k	1.07	0.90	0.91
4u	0.96	0.93	1.07

therapeutics at tumor sites. In our study, HSA's fluorescence at 315 nm decreased significantly with increasing **4k** and **4k** concentrations in the solution (Fig. 2). Fluorescence quenching experiments revealed that the bimolecular quenching constants (k_q) for the compounds were at least three orders of magnitude higher than the typical maximum diffusion-controlled rate constant for biomolecules (2×10^{10} L mol^{-1} s^{-1}). This observation suggests that static quenching is the dominant mechanism, implying the formation of stable HSA–**4k** and HSA–**4u** adducts.

Furthermore, the Stern–Volmer quenching constants (K_{sv}), bimolecular quenching constants (k_q), the binding constants (K_b) and the number of binding sites (n) were determined using the Stern-Volmer equation (Eq. 2) and Scatchard analysis (Eq. 3, Figs. S47 and S48), and the results are summarized in Table 3. These parameters provide additional support for the strong and specific binding interactions between our compounds and HSA.

$$\log[(I_0 - I)] = \log K_b + n\log[Q] \quad (3)$$

3.2.2.3. Competitive HSA binding studies with ibuprofen and Eosin markers. Understanding the specific binding interactions between drugs and proteins like HSA is crucial for the rational design of therapeutic agents. HSA, which plays a significant role in drug transport, features a heart-shaped tertiary structure composed of three homologous domains (I–III), each further divided into two subdomains: A and B. Of particular interest are subdomains IIA and IIIA, which are known to host primary drug-binding sites, commonly referred to as site I and site II, respectively.

In our study, we investigated the binding interactions of two newly synthesized pyrido-dipyrimidines, labeled **4k** and **4u**, with HSA. To determine their site-specific affinity, we conducted competitive binding assays using known site markers: Eosin Y for site I (subdomain IIA) and Ibuprofen for site II (subdomain IIIA). Both markers and HSA were prepared in equimolar concentrations (2 μM), and the examined compounds were introduced incrementally, up to a 2.5:1 molarratio relative

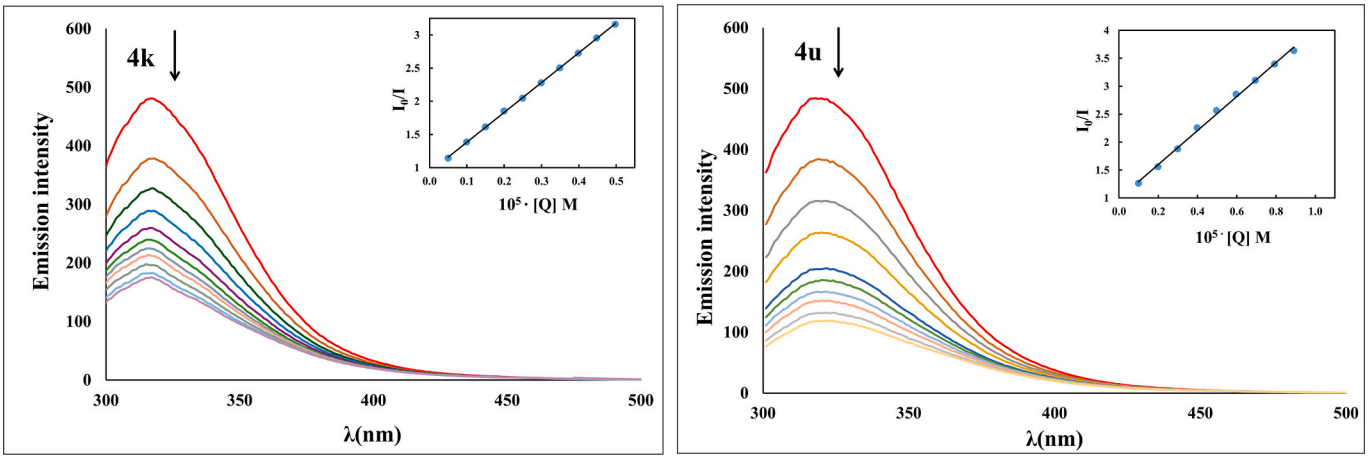

Fig. 3. Fluorescence spectra of HSA–ibuprofen in the absence (red lines) and presence of varying amounts of compounds **4k** and **4u**. Insert graphs: Stern–Volmer plots of HSA for compounds **4k** and **4u**. (For interpretation of the references to colour in this figure legend, the reader is referred to the web version of this article.)

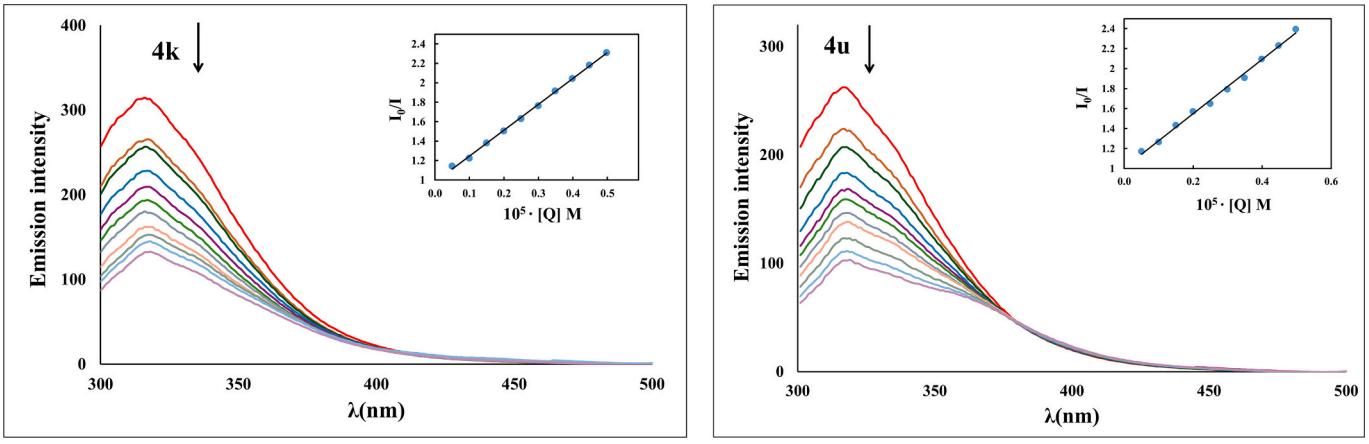

Fig. 4. Fluorescence spectra of HSA–Eosin Y in the absence (red lines) and presence of varying amounts of compounds **4k** and **4u**. Insert graphs: Stern–Volmer plots of HSA for compounds **4k** and **4u**. (For interpretation of the references to colour in this figure legend, the reader is referred to the web version of this article.)

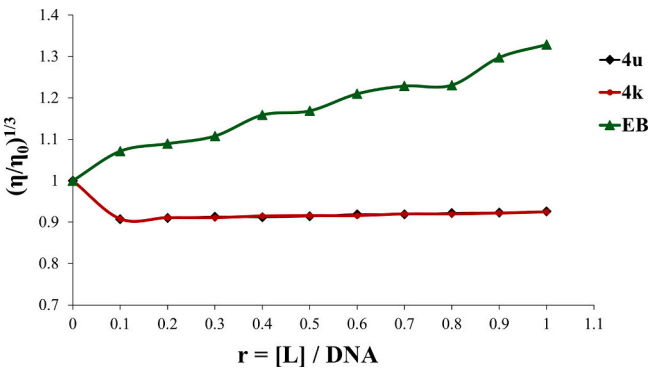

Fig. 5. Effect of increasing amounts of **EB** and ligands (**4k** and **4u**) on the relative viscosity of CT-DNA at 25.0 ± 0.2 °C.

Table 4
Concentrations of compounds that induced a 50% decrease in HeLa, K562, LS174, A549, and MRC-5 cell survival rate expressed as IC_{50} ± SD (μM).

Compound	HeLa	K562	LS174	A549	MRC-5
4a	63.29 ± 4.95	83.00 ± 8.75	138.59 ± 7.61	>200	140.30 ± 10.03
4b	24.36 ± 0.57	86.61 ± 5.92	139.44 ± 8.60	>200	127.28 ± 5.45
4c	147.61 ± 7.09	>200	>200	>200	>200
4d	23.20 ± 0.63	71.68 ± 5.81	179.94 ± 11.15	>200	>200
4e	26.33 ± 2.17	81.73 ± 5.88	192.47 ± 2.92	>200	>200
4f	27.28 ± 4.59	90.24 ± 2.83	186.30 ± 13.19	>200	166.83 ± 8.09
4g	104.79 ± 9.00	111.83 ± 6.57	171.50 ± 3.80	>200	>200
4h	53.42 ± 1.58	26.27 ± 8.28	122.42 ± 9.11	173.26 ± 9.01	176.21 ± 8.88
4i	74.20 ± 9.07	33.78 ± 9.77	171.70 ± 2.34	192.95 ± 8.06	>200
4j	40.63 ± 5.56	32.77 ± 0.20	124.63 ± 9.71	134.79 ± 1.10	58.25 ± 2.92
4k	9.82 ± 1.07	31.25 ± 6.81	110.64 ± 9.68	158.41 ± 7.74	122.31 ± 9.75
4l	113.18 ± 7.22	89.28 ± 22.88	184.23 ± 5.48	>200	>200
4m	91.23 ± 5.02	20.10 ± 1.65	140.93 ± 0.54	>200	149.58 ± 12.60
4n	146.49 ± 8.49	135.70 ± 0.64	>200	>200	>200
4o	122.05 ± 3.12	167.13 ± 7.93	126.22 ± 4.32	>200	186.57 ± 8.49
4p	86.76 ± 8.68	37.92 ± 8.53	102.15 ± 2.85	>200	140.90 ± 8.66
4q	110.53 ± 9.88	136.32 ± 4.02	178.06 ± 1.47	>200	>200
4r	146.85 ± 0.96	155.55 ± 8.99	181.03 ± 7.98	>200	>200
4s	144.78 ± 9.95	141.06 ± 3.72	166.44 ± 0.89	>200	>200
4t	77.61 ± 9.53	71.94 ± 0.68	131.29 ± 9.17	>200	172.48 ± 8.03
4u	98.06 ± 5.96	17.36 ± 1.39	165.03 ± 10.77	>200	159.69 ± 2.56
4v	74.20 ± 9.07	33.78 ± 9.77	171.70 ± 2.34	192.95 ± 8.06	>200
Cisplatin	2.64 ± 0.19	9.70 ± 0.70	20.77 ± 1.67	17.53 ± 2.06	21.28 ± 2.84

The table presents IC50 values of compounds expressed as the mean ± standard deviation of two independent experiments were performed in triplicate. IC50 value is defined as the concentration of an agent that inhibits cell survival by 50%, compared to the control cells.

to HSA.

Fluorescence titration experiments were performed using an excitation wavelength of 295 nm, and emission spectra were recorded between 300 and 500 nm. Upon formation of HSA-marker adducts (HSA–Eosin Y and HSA–Ibuprofen), strong fluorescence was observed, which diminished significantly as the complexes displaced the markers from their respective binding pockets. This displacement indicates effective competition and binding of the complexes to the same sites (Figs. 3 and 4**).**

The quenching of fluorescence was analyzed using both the Stern–Volmer (Eq. 2) and Scatchard equations (Eq. 3, Figs. S49-S52**).** In the Table 3 are presented the Stern–Volmer quenching constants (K_{sv}), bimolecular quenching constants (k_q), the binding constants (K_b) and the number of binding sites (n). The data reveal that both **4k** and **4u** interact with HSA at both site I and site II with strong affinity, characterized by binding constants on the order of 10^5 M^{-1}. These findings suggest that the complexes exhibit dual-site binding behavior on the HSA molecule.

3.2.3. *Viscosity*

While optical techniques are useful for investigating DNA interactions, they often fall short in conclusively determining the binding mode of **4k** and **4u**. In contrast, hydrodynamic measurements, particularly viscosity studies, offer a more definitive means of probing how compounds interact with DNA. Classical intercalation typically results in a marked increase in DNA solution viscosity, as the intercalating molecules insert between base pairs, thereby elongating the DNA helix. Conversely, non-classical or partial intercalation can introduce bends or kinks into the DNA structure, effectively shortening its contour length and leading to a decrease or negligible change in viscosity. Furthermore, compounds that bind through groove binding or electrostatic interactions generally exhibit minimal impact on DNA viscosity. In the current study, gradual addition of the **4k** and **4u** led to only a slight increase in the viscosity of the DNA solution (Fig. 5). Under the same experimental setup, EB a standard DNA intercalator, resulted in a significant enhancement of the relative viscosity of the DNA solution. Therefore, the observed viscosity behavior further supports the conclusion that **4k** and **4u** primarily engage with DNA *via* the groove binding mode.

3.3. *In vitro cytotoxic activity*

The cytotoxic activity against human malignant cell lines (HeLa, K562, LS174, A549) and human normal cell line (MRC-5) of the tested compounds are shown in Table 4 as IC_{50} values. All tested compounds showed concentration-dependent cytotoxicity against three malignant cell lines (HeLa, K562, LS174) with IC_{50} concentrations ranging from 9.82 to 192.47 μM, except for compound **4n** against LS174 cells. Several compounds from this series exhibited notable cytotoxic activity,

Table 5
Selectivity in the cytotoxic activity of the compounds against normal MRC-5 cells.

Compound	HeLa	K562
4a	2.22	1.69
4b	5.22	1.47
4d	>8.62	>2.79
4e	7.60	>2.45
4f	6.12	1.85
4h	>2.70	>5.92
4j	1.43	1.78
4k	12.46	3.91
4l	>1.77	>2.24
4m	1.64	7.44
4p	1.62	3.72
4t	2.22	2.40
4u	1.63	9.20
4v	3.30	6.71

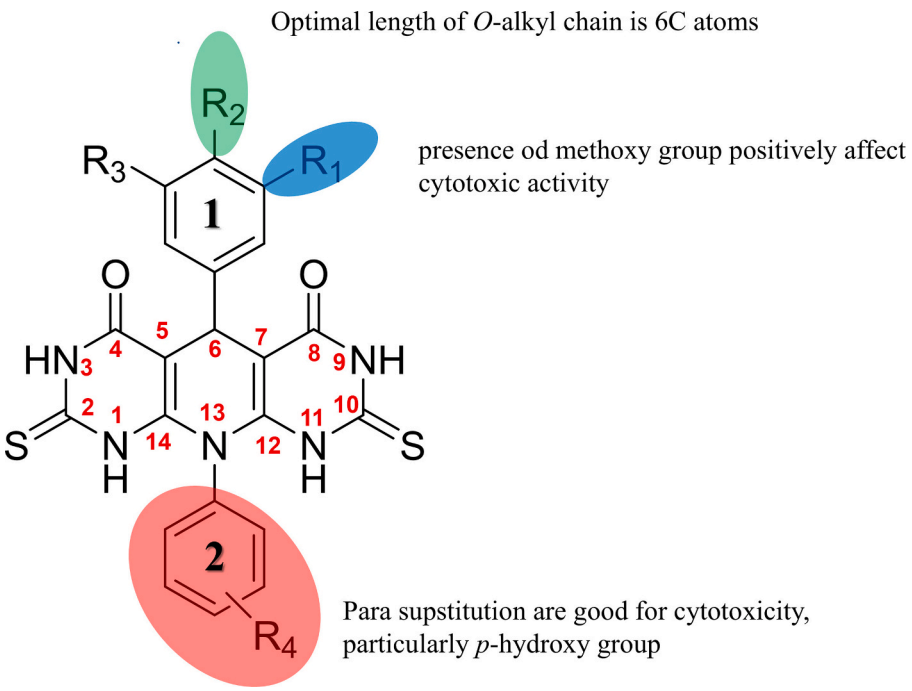

Fig. 6. SAR analysis.

whereas the remaining compounds displayed moderate to weak effects. HeLa and K562 cell lines exhibited the highest sensitivity to the tested compounds, with effective concentration of 9.82–146.85 μM for HeLa and 17.36–167.13 μM for K562. Compounds **4b**, **4d**, **4e** and **4f** showed significant cytotoxic activity against HeLa cell line (23.20–27.28 μM), while **4k** had the strongest cytotoxic activity against HeLa cell line (9.82 μM). The compounds **4a, 4h, 4j, 4v, 4p, 4t** also showed good, but more moderate, cytotoxic activity in the range from 40.63 to 86.76 μM. Compounds **4j, 4k, 4m, 4v, 4p** exhibited good cytotoxic activity (20.10–37.92 μM), while **4u** demonstrated the highest cytotoxic activity against K562 (17.36 μM). Moreover, a high selectivity in the cytotoxic activity was observed for the compound **4k** against HeLa cells when compared to its cytotoxicity against normal cells MRC-5, with selectivity coefficient of 12.46 (Table 5). In addition, compound **4u** showed selectivity index (SI) 9 against K562. Based on the obtained results, there were further investigated the mechanism of action of two compounds (**4u** and **4k**) that demonstrated the strongest anticancer activity and highest selectivity against HeLa and K562 cell lines respectively.

Table 6
The effect of the compound **4k** on the distribution of HeLa cells at specific phases of the cell cycle after 24 and 48 h at IC_{50} and 2 × IC_{50} concentrations.

24 h	Compound	SubG1%	G1%	S%	G2/M%
HeLa	**Control**	0.41 ± 0.02	50.61 ± 1.78	21.77 ± 0.95	27.76 ± 0.87
	IC_{50} 4k	7.59 ± 0.50	46.54 ± 1.65	27.47 ± 2.37	19.01 ± 1.74
	2 × IC_{50} 4k	9.41 ± 2.21	55.44 ± 2.87	19.26 ± 4.56	16.38 ± 5.90
48 h	**Compound**	**SubG1%**	**G1%**	**S%**	**G2/M%**
HeLa	**Control**	5.01 ± 5.06	52.60 ± 4.17	18.61 ± 8.51	24.25 ± 9.18
	IC_{50} 4k	10.82 ± 1.72	45.79 ± 2.74	16.97 ± 1.16	26.86 ± 1.57
	2 × IC_{50} 4k	11.52 ± 1.41	44.61 ± 2.27	20.18 ± 1.01	24.17 ± 1.83

The table presents the percentage of cells in the subG1, G1, S, and G2/M phases of the cell cycle, expressed as the mean ± standard deviation of three independent experiments.

Hydrolytic stability studies of compound **4u** were conducted by monitoring solutions in DMSO-d_6, DMSO-d_6/D_2O, and DMSO-d_6/D_2O with PBS (phosphate-buffered saline) *via* ^{1}H NMR spectroscopy. Due to the addition of D_2O, H/D isotopic exchange of labile protons is observed in **Figs. S53b** and **S53c**. Nevertheless, the diagnostic benzylic methine proton ($\delta \approx 5.9$ ppm, singlet) persists unchanged across all conditions. This indicates that the PDP tricyclic core in **4u** remains intact and resistant to hydrolysis over the 72-h monitoring period.

3.4. SAR study

The synthesized compounds share a common pyrido[2,3-*d*:6,5-*d*']dipyrimidine-4,6(1*H*,7*H*)-dione scaffold with structural variations in the amine and aldehyde residues, which appear to significantly influence their cytotoxic activity (Fig. 6). As shown in Table 4, most of the compounds demonstrated notable activity against HeLa and K562 cell lines, whereas A549 cells exhibited limited sensitivity. All derivatives contain the same tricyclic core, and differences in their biological activity can be primarily attributed to the nature and position of aryl substituents.

The analysis of substituents at position 5 on the phenyl ring shows that the presence of *para*-hydroxy groups, as in compounds **4h**, **4i**, **4k**, **4p**, **4u** and **4v** correlates with enhanced activity, particularly against K562 and, in the case of **4v**, also against HeLa cells. This improvement is likely related to the hydrogen-bonding capacity of the hydroxyl group, which may strengthen interactions with the biological target and increase affinity. Compound **4d**, which carries a *para*-methyl group, also shows good activity toward HeLa but reduced potency against K562. These results suggest that electron-donating groups can enhance activity, but hydrogen-bonding ability has a more decisive impact on both potency and selectivity. Substituents at position 10 in phenyl ring also play a crucial role in modulating biological response. Bulky phenoxy group, as in compounds **4b** and **4f**, result in moderate activity toward HeLa cells but weak or no activity against other cell lines, indicating that increased lipophilicity and steric bulk may enhance interactions with specific hydrophobic sites but reduce broader activity. All active compounds contain a thiocarbonyl group at position 2, which remains constant across the series and likely contributes to a baseline level of biological activity through hydrogen bonding or coordination with

Table 7
The effect of the compound **4u** on the distribution of K562 cells at specific phases of the cell cycle after 24 and 48 h at IC_{50} and 2 × IC_{50} concentrations.

24 h	Compound	SubG1%	G1%	S%	G2/M%
K562	**Control**	8.94 ± 1.51	40.13 ± 2.92	22.75 ± 2.64	28.81 ± 1.79
	IC_{50} 4u	17.77 ± 5.94	38.42 ± 2.48	21.90 ± 0.76	22.66 ± 6.99
	2 × IC_{50} 4u	40.03 ± 0.33	33.60 ± 0.28	15.69 ± 0.44	11.41 ± 0.92
48 h	**Compound**	**SubG1%**	**G1%**	**S%**	**G2/M%**
K562	**Control**	8.19 ± 6.59	42.90 ± 3.88	24.20 ± 5.41	25.49 ± 3.99
	IC_{50} 4u	17.31 ± 8.31	40.11 ± 1.40	20.32 ± 3.75	23.00 ± 5.66
	2 × IC_{50} 4u	41.38 ± 3.62	37.86 ± 4.86	14.26 ± 1.05	7.14 ± 0.80

The table presents the percentage of cells in the subG1, G1, S, and G2/M phases of the cell cycle, expressed as the mean ± standard deviation of three independent experiments.

metal ions in enzyme active sites.

Overall, the structure–activity relationship indicates that *para*-hydroxyphenyl groups at position 5′ enhance activity, especially against leukemia cells, while substituents at position 10 strongly influence both potency and selectivity. These findings suggest that further optimization should focus on systematic modification of aryl substituents at positions 5 and 10 to fine-tune electronic properties, hydrophilicity, and steric factors in order to achieve improved cytotoxic potency and selectivity.

3.5. Cell cycle analysis

The compounds (**4k** and **4u**) that showed the most potent cytotoxic activity against Hela and K562 cells were further analyzed for the effect on cell cycle distribution. Flow cytometry analysis utilizing propidium iodide for DNA labeling was used for investigation of the mechanism of action of these compounds. Results are presented in Tables 6 and 7 and Figs. 7 and 8.

Obtained data showed that compound **4k** caused noticeable increase in the proportion of HeLa cells in the SubG1 phase of the cell cycle when applied at the IC_{50} concentration for 24 h (7.59 ± 0.50%, compared with control 0.41 ± 0.02%), as well as at 2 × IC_{50} concentration (9.41 ± 2.21%, compared with control 0.41 ± 0.02%). A similar trend of accumulation of the cells in the SubG1 phase was also observed when compound **4k** was applied at the IC_{50} concentration for 48 h (10.82 ± 1.72%, compared with control 5.01 ± 5.06%), as well as at 2 × IC_{50} concentration (11.52 ± 1.41%, compared with control 5.01 ± 5.06%).

Compound **4u** exhibited observable increase in the proportion of K562 cells in the SubG1 phase of the cell cycle when applied at the IC_{50} concentration for 24 h (17.77 ± 5.94%, compared with control 8.94 ± 1.51%), as well as at 2 × IC_{50} concentration (40.03 ± 0.33%, compared with control 8.94 ± 1.51%). Again, a comparable upward trend was detected when the compound **4u** was used at the IC_{50} concentration for 48 h (17.31 ± 8.31%, compared with control 8.19 ± 6.59%), as well as at 2 × IC_{50} concentration (41.38 ± 3.62%, compared with control 8.19 ± 6.59%).

Results of the cell cycle analysis suggest that compounds **4k** and **4u** induced proapoptotic effect on HeLa and K562 cells respectively, both, after 24 and 48 h of incubation, as well as, in both tested concentrations of the compounds IC_{50} and 2 × IC_{50}.

3.6. Fluorescence microscopy for apoptosis assessment

The pro-apoptotic effect of the compounds (**4k** and **4u**) was further evaluated by examining morphological changes in HeLa and K562 cells

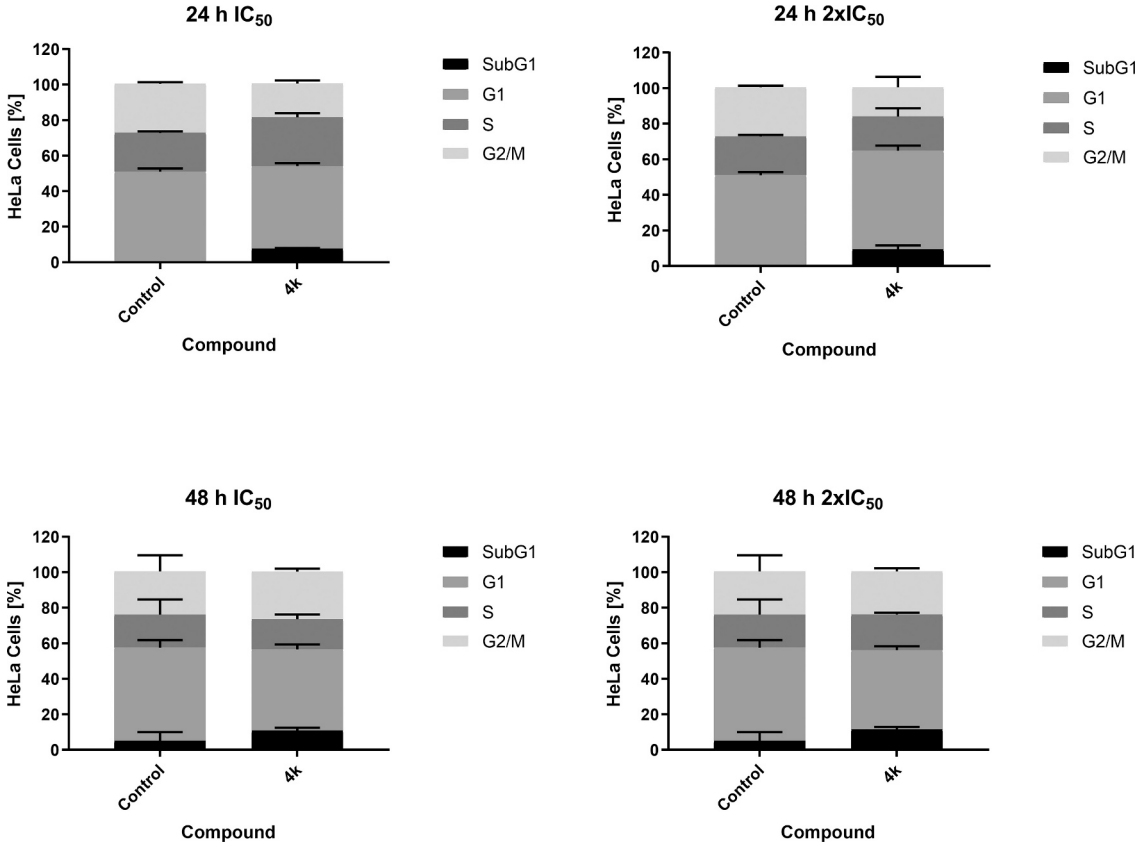

Fig. 7. Cell cycle changes in phase distribution of HeLa cells induced by **4k** compound after 24 h and 48 h treatment.

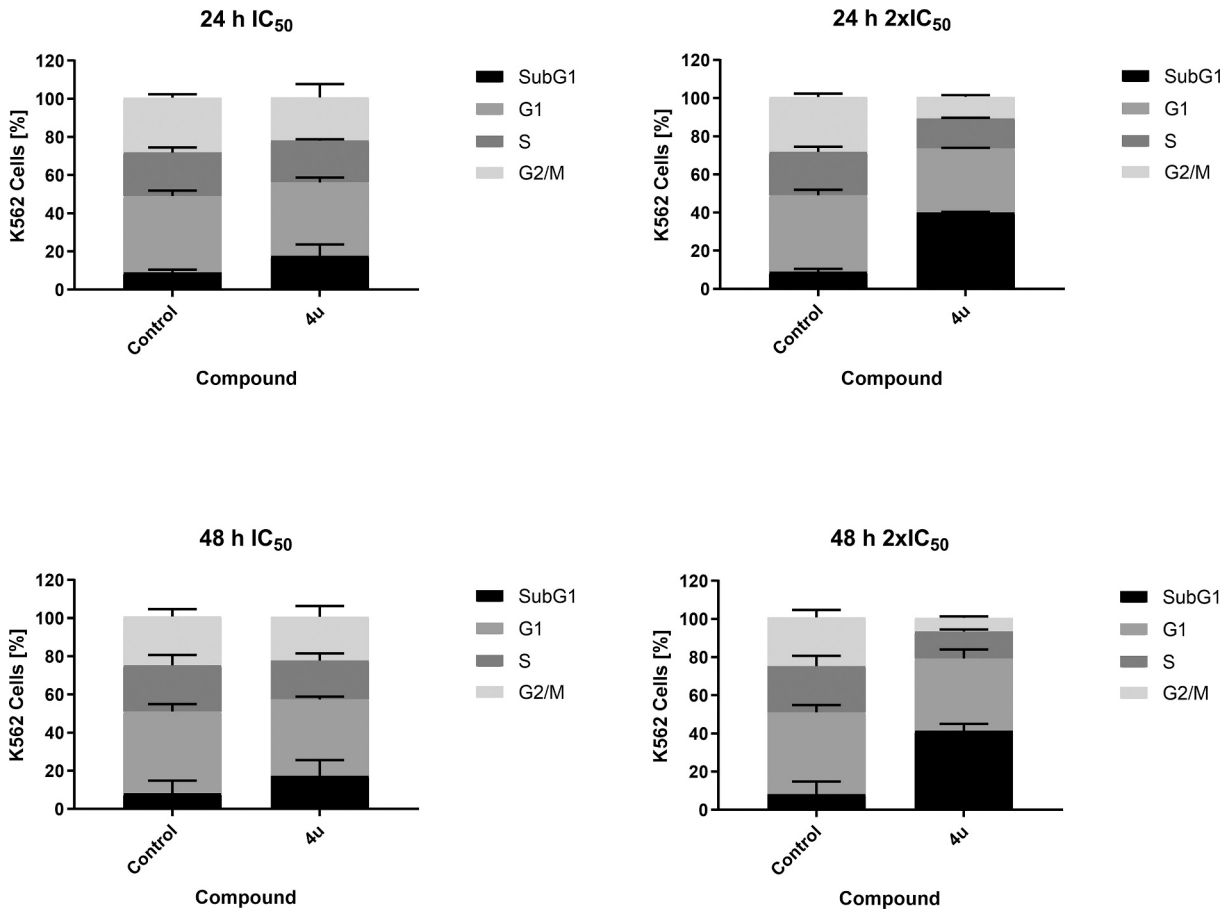

Fig. 8. Cell cycle changes in phase distribution of K562 cells induced by **4u** compound after 24 h and 48 h treatment.

using acridine orange/ethidium bromide (AO/EB) staining and fluorescence microscopy. Cells were treated for 48 h with each respective compound at its IC_{50} and 2 × IC_{50} concentrations.

After observing Hela cells, attached on the coverslips, after treatment with **4k** compound of both IC_{50} and 2 × IC_{50} concentrations, the cells showed distinct features of apoptosis (Fig. 9). The cells were predominantly stained green, indicating that their cell membranes were still intact. However, their nuclei contained condensed and fragmented chromatin, a key sign of early apoptosis. Additionally, the formation of apoptotic bodies through membrane blebbing was clearly visible. After analyzing supernatant of Hela cells, we can see, also, clear signs of apoptosis, rounded cells with membrane blebbing and a small fraction of cells stained red, signifying progression to late-stage apoptosis or secondary necrosis.

Morphological analysis was also conducted on K562 cells following treatment with compound **4u** at both IC_{50} and 2 × IC_{50} concentrations for 48 h (Fig. 10).The results closely mirrored the effects observed in HeLa cells, confirming a pro-apoptotic response. The majority of the K562 cell population displayed distinct characteristics apoptosis. Although the cells predominantly stained green with acridine orange, indicating their cell membranes remained intact, their nuclei showed clear evidence of condensation and fragmentation, which are key hallmarks of apoptosis. Furthermore, extensive membrane blebbing and the formation of apoptotic bodies were readily visible. A smaller portion of the cell population was stained orange-red with ethidium bromide, signifying a loss of membrane integrity as cells progressed into late-stage apoptosis or secondary necrosis.

These observations confirm that compounds **4k** and **4u** induced cell death in HeLa and K562 cells through a morphologically similar apoptotic mechanism.

3.7. *Effect of 4k and 4u on Intracellular ROS Levels*

To further explore the signaling context, intracellular ROS production was measured after 24 h. Compound **4k** prompted a 1.52 ± 0.15-fold increase in ROS levels in HeLa cells. In K562 cells treated with **4u**, a discreet but consistent elevation in fluorescence intensity was observed, corresponding to a 1.07 ± 0.08-fold shift relative to the control. These observations were supported by the 3.86 ± 0.44-fold and 1.37 ± 0.19-fold increases recorded for the positive control H_2O_2 in HeLa and K562, respectively). These data suggest that ROS generation acts as an early signaling event for both analogs, regardless of their downstream caspase dependency (Fig. 11).

3.8. *Caspase activities*

Although compounds **4k** and **4u** share the same pyrido-dipyrimidine core, our results indicate significant differences in the mode of apoptotic response. Both compounds increased the SubG1 population and induced typical apoptotic morphology, but their dependence on caspase activity and oxidative stress profiles differed significantly. For compound **4k** (Table S1), tested in HeLa cells, pre-treatment with inhibitors of caspase-3, -8, and -9 led to a substantial reduction in the SubG1 population (from 22.19% to levels between 1.69% and 3.18%), demonstrating that **4k** activates classical intrinsic and extrinsic apoptotic pathways (Fig. 12). This caspase-dependent execution is accompanied by a 1.52 ±0.15-fold increase in intracellular ROS levels at 24 h. In contrast, the data obtained for **4u** in K562 cells show that the same inhibitors did not significantly reduce the subdiploid DNA content (13.38% alone *vs.* 10.35-19.39% with inhibitors), confirming that **4u** induces apoptosis through a caspase-independent pathway (Fig. 13). In this model, a

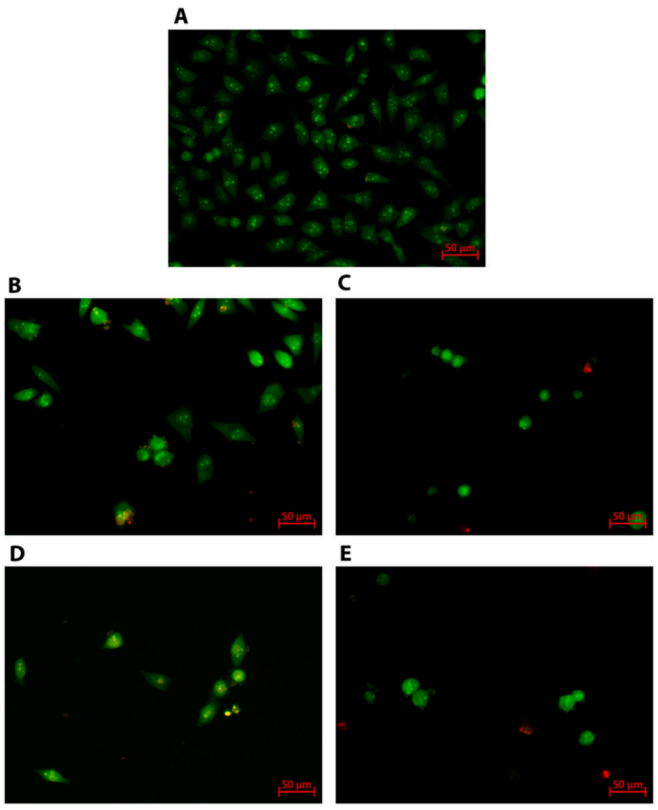

Fig. 9. Representative fluorescence photomicrographs of acridine orange/ethidium bromide-stained HeLa cells after 48 h treatment with **4k** compound of IC_{50} and 2 × IC_{50} concentrations. A) control, B) treatment with IC_{50} concentration C) treatment with IC_{50} concentration – supernatant, D) treatment with 2 × IC_{50} concentration and E) treatment with 2 × IC_{50} concentration – supernatant.

discreet but consistent pro-oxidative trend was observed, with a 1.07 ±0.08-fold elevation in ROS levels, suggesting that ROS generation may act as a supplementary signaling event in the caspase-independent death process. This divergence can be rationalized by subtle structural differences and cell-line-specific responses. The flexible, lipophilic hexyloxy substituent in **4k** increases conformational adaptability, which may favor the engagement of the classical caspase cascade in HeLa cells. Conversely, **4u**, bearing a compact, halogen-substituted moiety and a hydroxyl group, triggers a programmed cell death response that proceeds independently of caspase-3, -8, and - 9 activity in K562 cells, potentially utilizing the observed discreet ROS induction as an alternative upstream trigger. Overall, these findings demonstrate that small structural modifications within the same scaffold can modulate the biochemical route of the apoptotic response without altering the final pro-apoptotic outcome.

3.9. Molecular docking simulation

By considering the possibility of deprotonation of the tested compounds under physiological conditions, it was found that the neutral form of the molecule **4u** at pH 7.4 is present in an amount of 47.0%. The monoanion (**4u-A**) formed by the departure of a hydrogen ion from the nitrogen atom of the central pyrido-dipyrimidine part of the molecule is present in an amount of 27.9% under these conditions. The molecule **4k** at pH 7.4 in its neutral form is present in an amount of 49.9%, while the corresponding monoanion forms formed by deprotonation of the nitrogen atoms are present in an amount of 29.6% (**4k-A1**) and 11.6% (**4k-A2**) separately. The other proposed ionic forms of both the molecule **4u** and the molecule **4k** are present in an amount of less than 10% under physiological conditions and are not considered further (Fig. 14).

Although the molecular docking analysis considered 10 possible binding positions of DNA molecule, only the positions with the strongest connections, both in the minor groove and in the major groove of the DNA molecule, will be taken into account for all the ligands considered.

Considering the values of the corresponding thermodynamic parameters presented in Table 8, it can be observed that the DNA molecule is more strongly inhibited by the binding of the corresponding ligands in the minor groove position than in the major groove position. When bound to the minor groove position of the observed DNA molecule, the **4k** molecule, particularly its **4k-A2** anion, exhibits greater inhibitory activity than any form of the **4u** molecule. Inhibition of the DNA molecule by ligand binding in the major groove position is more pronounced in the case of the **4u** species, specifically in its anionic form, than in any form of the **4k** molecule. It can be observed that the difference in ΔG_{bind} and K_i values between complexes formed by ligand binding in the minor groove and major groove positions is smaller for the **4u** molecule than for the **4k** molecule, which is a consequence of the bulkiness of these ligands. The HSA molecule can be inhibited more effectively by the **4k** molecule than by the **4u** molecule. The ionic forms of the **4k** molecule, particularly the **4k-A2** ion, are especially effective inhibitors of the HSA molecule. On the other hand, although the **4u** molecule is a weaker inhibitor of HSA than **4k**, its neutral form inhibits this protein more effectively than its anion (Fig. 15).

The inhibitory potential of the considered ligands is a consequence of the interactions that these ligands establish with the examined target molecule. In the case of both examined ligand molecules, the neutral form is dominant at physiological pH. Therefore, more detailed observations will be provided for the mentioned neutral forms of ligands. Data regarding the types of interactions established during the molecular docking analysis of the considered ionic forms of the ligands and the selected target molecules are provided in the Supplementary material. In the case of the most stable complex that **4u** forms with the DNA molecule in the minor groove position, this ligand interacts with the DNA molecule through nucleotides containing guanine (G), adenine (A), and cytosine (C). The following nucleotides belong to polynucleotide chain A: C1009, G1010, and C1011, while polynucleotide chain B includes nucleotides G2016, A2017, and A2018. When forming a complex with the DNA molecule by binding in the major groove position, the **4u** molecule interacts through nucleotides containing guanine (G), thymine (T), and cytosine (C). Among the mentioned nucleotides, polynucleotide chain A includes T1008, C1009, and G1010, while polynucleotide chain B includes nucleotides C2013, G2014, and C2015. The 4k molecule, when forming a complex with the DNA molecule in the minor groove position, establishes interactions with nucleotides T1008, C1009, and G1010 of polynucleotide chain A, and with nucleotides C2013, G2014, and C2015 of polynucleotide chain B. When forming a complex with the DNA molecule in the major groove position, this ligand binds through nucleotides belonging to chain B: A2017, A2018, and T2019.

The fact that, in many cases, the same nucleotides participate in the formation of the most stable complex between the considered ligands and the DNA molecule, both when the ligand is positioned in the minor groove and when it is positioned in the major groove, indicates that this particular region of the DNA molecule is the most susceptible to forming target–ligand complexes. The formation of the target–ligand complex in the minor groove position is primarily contributed to by conventional and carbon hydrogen bonds, followed by π–anion, π–sulfur, and π–alkyl interactions. In addition to these, when the ligand is positioned in the major groove, π–donor hydrogen bonds and π–σ interactions also contribute to complex formation.

Considering the possibility of inhibiting HSA with molecule **4u**, it was determined that, in the most stable protein–ligand complex, interactions are established between the ligand and the following amino acids of this protein: Tyr150, Glu188, Ser192, Lys195, Gln196, Leu238, Val241, His242, Arg257, Ala291, and Glu292. With this protein, molecule **4k** interacts through the amino acids Tyr150, Glu188, Ser192,

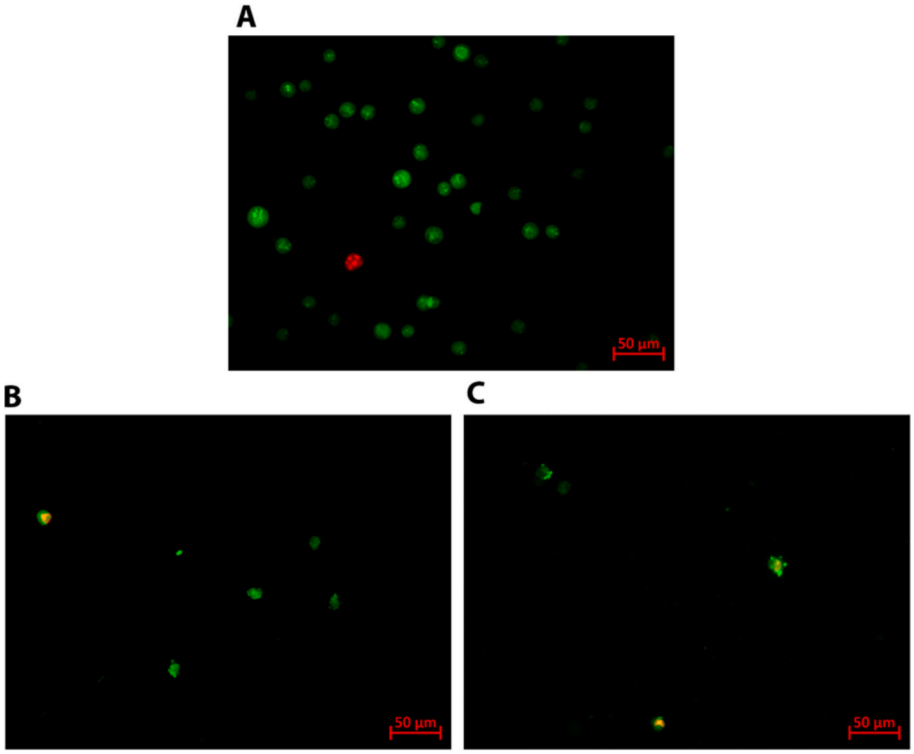

Fig. 10. Representative fluorescence photomicrographs of acridine orange/ethidium bromide-stained K562 cells after 48 h treatment with **4u** compound of IC_{50} and 2 × IC_{50} concentrations. A) control, B) treatment with IC_{50} concentration and C) treatment with 2 × IC_{50} concentration.

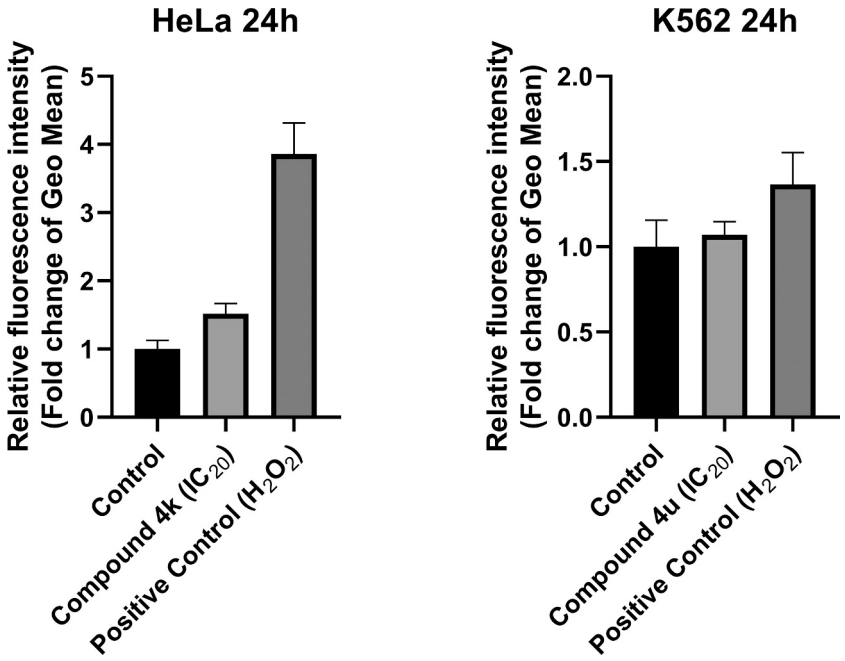

Fig. 11. Relative ROS levels in HeLa and K562 cells. Cells were treated with compound **4k** and **4u** (IC_{20}) for 24 h. ROS production was quantified by flow cytometry using DCFH-DA staining. Results are presented as the fold change of the fluorescence intensity geometric mean (Geo Mean) relative to the control (set to 1.0). Data represent the mean ± SD of values obtained from experimental triplicates (n=3). H_2O_2 (100 µM, 30 min) was used as a positive control.

Lys195, Gln196, His242, Arg257, Leu260, Ala261, Ile264, Ile290, Ala291, and Glu292. The fact that both ligands form their most stable complexes with the HSA molecule through as many as nine identical amino acids confirms the conclusion that both ligands bind to the same active site of the HSA molecule (Fig. 15). The interactions that contribute to the formation of these protein–ligand complexes are conventional and carbon hydrogen bonds, as well as π–donor hydrogen bonds, along with interactions involving π electrons, such as π–cation, π–anion, π–σ, π–sulfur, π–alkyl, and π–π stacked interactions (Table 9).

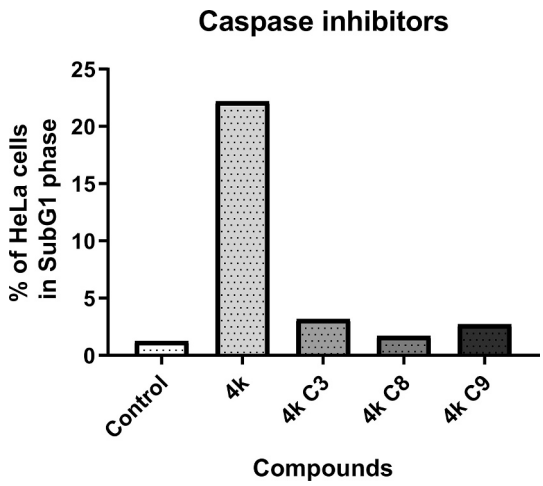

Fig. 12. The percentage of HeLa cells in the subG1 phase of the cell cycle determined for control, samples treated with the 4 k compound alone, as well as for samples treated with the compound followed by caspase-3, -–8, and -– 9 inhibitors (control; compound; C3– caspase-3 inhibitor; C8 – caspase-8 inhibitor; C9 – caspase-9 inhibitor).

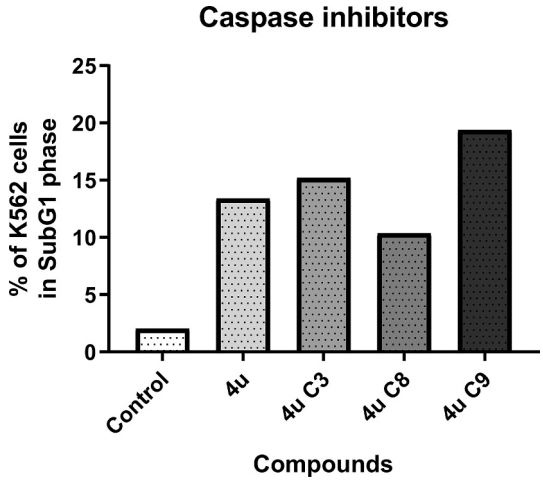

Fig. 13. The percentage of K562 cells in the subG1 phase of the cell cycle determined for control, samples treated with the 4u compound alone, as well as for samples treated with the compound followed by caspase-3, -8, and -9 inhibitors (control; compound; C3– caspase-3 inhibitor; C8 – caspase-8 inhibitor; C9 – caspase-9 inhibitor).

3.10. Molecular dynamics simulation

This study utilized molecular dynamics (MD) simulations to examine the conformational changes and stability of a receptor (DNA and HSA) in the presence of two different ligands, **4k** and **4u**. Key parameters, including root mean square deviation (RMSD), root mean square fluctuation (RMSF), and radius of gyration (Rg), were analyzed to evaluate the impact of ligands on the stability and flexibility of the protein structure. To evaluate the structural stability and conformational dynamics of DNA and HSA complexes, RMSD analyses were performed on trajectories obtained from 50 ns molecular dynamics MD simulations. RMSD is a key indicator that reflects the average atomic displacement relative to a reference structure over simulation time, thereby providing insight into the system's equilibration and flexibility. RMSD trajectories of DNA were analyzed under five conditions: unmodified DNA (DNA), DNA complexed in the major groove with **4k** (**DNAmajor4k**) and **4u** (**DNAmajor4u**), and DNA modified in the minor groove with **4k** (**DNAminor4k**) and **4u** (**DNAminor4u**). As shown in Fig. 16 (left), the

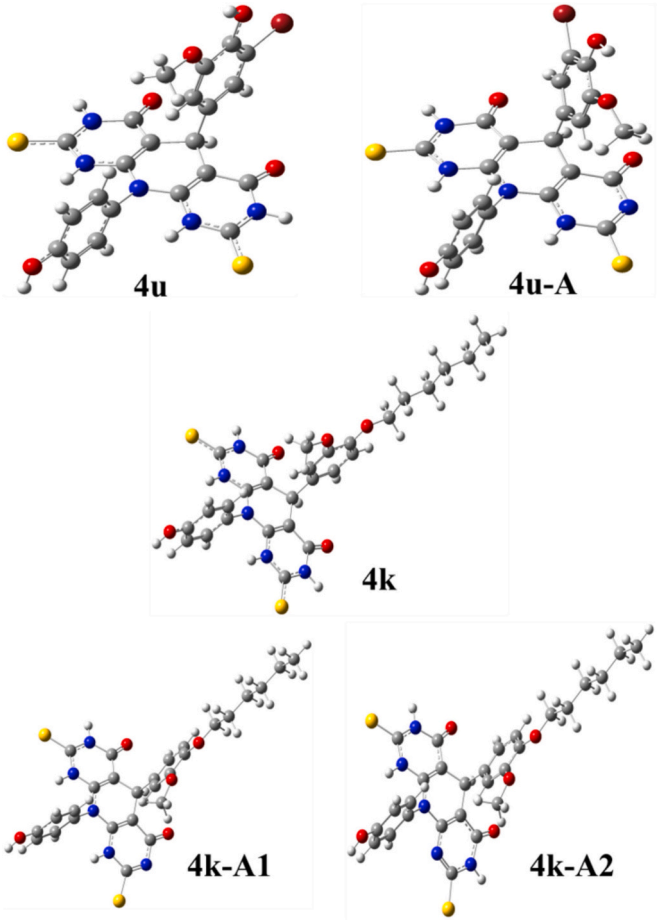

Fig. 14. Optimized geometries of neutral and ionic formed of **4u** and **4k** molecules and their ionic moieties, here estimated as ligands in the molecular docking simulation.

RMSD values for all DNA systems remained within a narrow band of approximately 1.0 to 4.5 Å throughout the 50 ns simulation. Ligand RMSD values calculated relative to the initial docked conformations after alignment of the DNA backbone for ligands **4k** and **4u** bound in the DNA major and minor grooves. Both ligands, **4k** and **4u**, exhibit stable RMSD values with fluctuations predominantly below ~3 Å throughout the simulation, with no abrupt increases indicative of ligand dissociation. An initial rapid increase in RMSD was observed during the first 3–5 ns, indicating system equilibration, where the DNA molecules transition from their initial minimized conformations to a more energetically stable state under dynamic conditions. After equilibration, the RMSD curves showed minor fluctuations, indicating that the DNA structures had reached relatively stable conformations. The close overlap and similar RMSD trajectories among the five DNA complexes (**DNA**, **DNAmajor4k**, **DNAmajor4u**, **DNAminor4k**, **DNAminor4u**) suggest that neither the groove-specific modifications nor the associated ligand binding caused significant perturbations to the overall DNA conformation. This stability is consistent with the intrinsic rigidity of the double helical DNA structure, which tends to resist large conformational deviations under physiological conditions. In contrast, RMSD trajectories for HSA protein complexes (Fig. 16, right) exhibited distinct behavior. Three HSA conditions were monitored: free HSA (HSA), and HSA complexed with **4k** (**HSA4k**) and **4u** (**HSA4u**). The RMSD values increased sharply during the initial 10 ns, reaching peak deviations between 5.0 and 5.5 Å. This initial phase likely reflects considerable structural rearrangements as the protein relaxes and adapts to the simulation environment, including possible side-chain reorientations and loop flexibility. Following the initial equilibration, the RMSD values

Table 8
Thermodynamic parameters corresponding to the most stable conformation of the target-ligand complex obtained by docking analysis. The labels "MIN" and "MAJ" in the index indicate that the corresponding ligand is bound in the minor or major groove position of the 1M6F molecule. The inhibition constant values (K_i) are presented in μM, while all energy values are presented in kcal/mol.

Complex	ΔG_{bind}	K_i	ΔG_{inter}	$\Delta G_{vdw+hbond+desolv}$	ΔG_{elec}	ΔG_{total}	ΔG_{tor}	ΔG_{unb}
1M6F-**4u**$_{MIN}$	−6.67	12.88	−8.04	−8.03	−0.01	−1.83	1.37	−1.83
1M6F-**4u**$_{MAJ}$	−5.82	53.81	−7.20	−6.93	−0.26	−1.91	1.37	−1.91
1M6F-**4u-A**$_{MIN}$	−6.74	11.38	−8.12	−7.83	−0.29	−1.99	1.37	−1.99
1M6F-**4u-A**$_{MAJ}$	−5.90	47.69	−7.27	−6.97	−0.29	−2.15	1.37	−2.15
1M6F-**4k**$_{MIN}$	−7.28	4.59	−10.27	−9.91	−0.36	−1.57	2.98	−1.57
1M6F-**4k**$_{MAJ}$	−4.90	256.95	−7.88	−7.55	−0.33	−2.94	2.98	−2.94
1M6F-**4k-A1**$_{MIN}$	−5.62	75.94	−8.60	−8.16	−0.44	−2.86	2.98	−2.86
1M6F-**4k-A1**$_{MAJ}$	−4.68	373.87	−7.66	−7.59	−0.07	−2.70	2.98	−2.70
1M6F-**4k-A2**$_{MIN}$	−7.83	1.82	−10.81	−10.48	−0.34	−2.14	2.98	−2.14
1M6F-**4k-A2**$_{MAJ}$	−4.83	286.11	−7.82	−7.52	−0.29	−3.28	2.98	−3.28
7DJN-**4u**	−7.17	5.58	−8.54	−8.29	−0.25	−1.61	1.37	−1.61
7DJN-**4u-A**	−6.88	9.01	−8.26	−7.96	−0.29	−1.89	1.37	−1.89
7DJN-**4k**	−8.30	822.23	−11.28	−11.23	−0.05	−1.76	2.98	−1.76
7DJN-**4k-A1**	−8.35	761.23	−11.33	−10.95	−0.38	−1.70	2.98	−1.70
7DJN-**4k-A2**	−8.54	551.33	−1.52	−11.47	−0.05	−2.25	2.98	−2.25

fluctuated moderately within a range of approximately 3.0 to 5.0 Å for the remainder of the simulation. This behavior indicates that HSA complexes possess significant conformational flexibility and dynamic fluctuations. Backbone RMSD profiles of HSA and the corresponding HSA–ligand complexes with ligands **4k** and **4u**, showing moderate conformational fluctuations (up to ~5 Å) characteristic of HSA flexibility. Importantly, these backbone motions do not translate into increased ligand RMSD, confirming stable ligand binding within the HSA binding site during the entire simulation time. The similarity among the RMSD trajectories of the three HSA complexes (**HSA**, **HSA4k** and **HSA4u**) indicates that the modifications or binding of examined ligands do not drastically alter the overall protein stability. Importantly, these backbone motions do not translate into increased ligand RMSD, confirming stable ligand binding within the HSA binding site during the entire simulation time.

Comparative evaluation of DNA and HSA RMSD data reveals distinct dynamic signatures reflecting their differing structural roles. DNA exhibits lower RMSD fluctuations and maintains structural integrity more rigidly throughout the simulation, consistent with its role as a stable genetic material. On the other hand, HSA shows higher RMSD values and greater conformational variability, reflecting the functional necessity for protein flexibility in ligand binding and allosteric regulation. The equilibration times for both systems were within the first 10 ns, indicating rapid adaptation to the simulation conditions. These results highlight the differential impact of molecular environment and modifications on the dynamic stability of nucleic acids *versus* proteins.

RMSF analysis (Fig. 17) revealed clear differences in residue-specific flexibility between DNA and HSA complexes. In DNA-associated complexes (Fig. 17, left), most residues exhibited moderate fluctuations (~28–32 Å) with a pronounced peak in the N-terminal region (~residues 1–50) reaching ~34–39 Å in the case of the **DNAmajor4u** (green line). Also, these behaviours for residues 1–50 are noticed for **DNAminor4u** and **DNAmajor4k** in ranges 15-19 Å and 15-24 Å, respectively. Beyond this, the fluctuation remained relatively flat, and no major variation was observed between examined complexes. This indicates that neither the interaction mode nor ligand association significantly altered the global dynamic stability of the DNA-ligand complexes. In contrast, HSA systems (Fig. 17, right) showed considerably lower RMSF amplitudes (predominantly 1–6 Å), indicative of greater overall structural rigidity. However, several distinct local peaks were detected, notably around residues ~60, ~150, ~250, ~550–600, ~700, and ~900, with peak values reaching approximately 5–6 Å. These regions likely correspond to flexible loops or solvent-exposed domains implicated in ligand recognition and transport. The ligand-bound forms (**HSA4k** and **HSA4u**, represented by yellow and green lines, respectively) displayed slightly increased RMSF amplitudes at specific residues compared to the unbound protein, indicating that ligand binding induces localized flexibility changes while preserving the overall protein fold. Furthermore, these findings demonstrate that while HSA maintains its rigid structure with movement concentrated in particular functional locations, DNA complexes have greater intrinsic mobility, mostly because of terminal flexibility.

In this study, Rg was evaluated for free DNA, DNA bound with ligands **4k** and **4u** at major and minor grooves, and HSA in both free and ligand-bound forms, over 50 ns simulations, allowing a direct comparison of structural behavior under varying binding conditions. For DNA-containing systems (Fig. 18, left), Rg values remained consistently within 13.8–15.2 Å. This narrow range indicates that the DNA maintains its global structural integrity regardless of ligand-binding site (major or minor groove). Notably, no long-term trends toward compaction or expansion were observed, suggesting that ligand binding does not significantly perturb the canonical B-form double helix. Minor fluctuations are attributable to normal base-pair breathing motions and inherent helical flexibility. Importantly, no abrupt deviations in Rg occurred, implying that ligand association is compatible with the native DNA conformation and does not induce denaturation or large-scale unwinding.

HSA complexes (Fig. 18, right) exhibited Rg values ranging from 38.5 to 41.0 Å. A transient increase during the first ~5 ns likely corresponds to conformational relaxation as the protein adapts to the simulation environment and, in the ligand-bound cases (**HSA4k** and **HSA4u**), to ligand accommodation. After this initial equilibration, Rg values stabilized, demonstrating that HSA maintains its tertiary structural compactness. Ligand-bound HSA forms displayed Rg profiles similar to the unbound protein, indicating that ligand binding occurs without substantial disruption of the overall conformation. Localized conformational adjustments are likely confined to binding pockets. The similarity in Rg trends between free and ligand-bound states for both DNA and HSA underscores the intrinsic structural resilience of these biomolecules. Ligand binding induces only local conformational changes at specific sites, without altering global compactness. The absence of major unfolding or aggregation events during the 50 ns simulations further confirms the stability of these systems. Functionally, the preservation of global structural stability has important implications. For DNA, it indicates that ligand interactions may modulate local binding regions without compromising the molecule's overall biological function. For HSA, maintenance of compactness supports its physiological role as a transport protein, as significant unfolding could negatively affect ligand affinity, binding kinetics, and transport efficiency. In addition, these Rg analyses suggest that, under the simulated conditions, ligand binding does not destabilize the global structure of either DNA or HSA.

To further correlate the MD simulation results with experimental

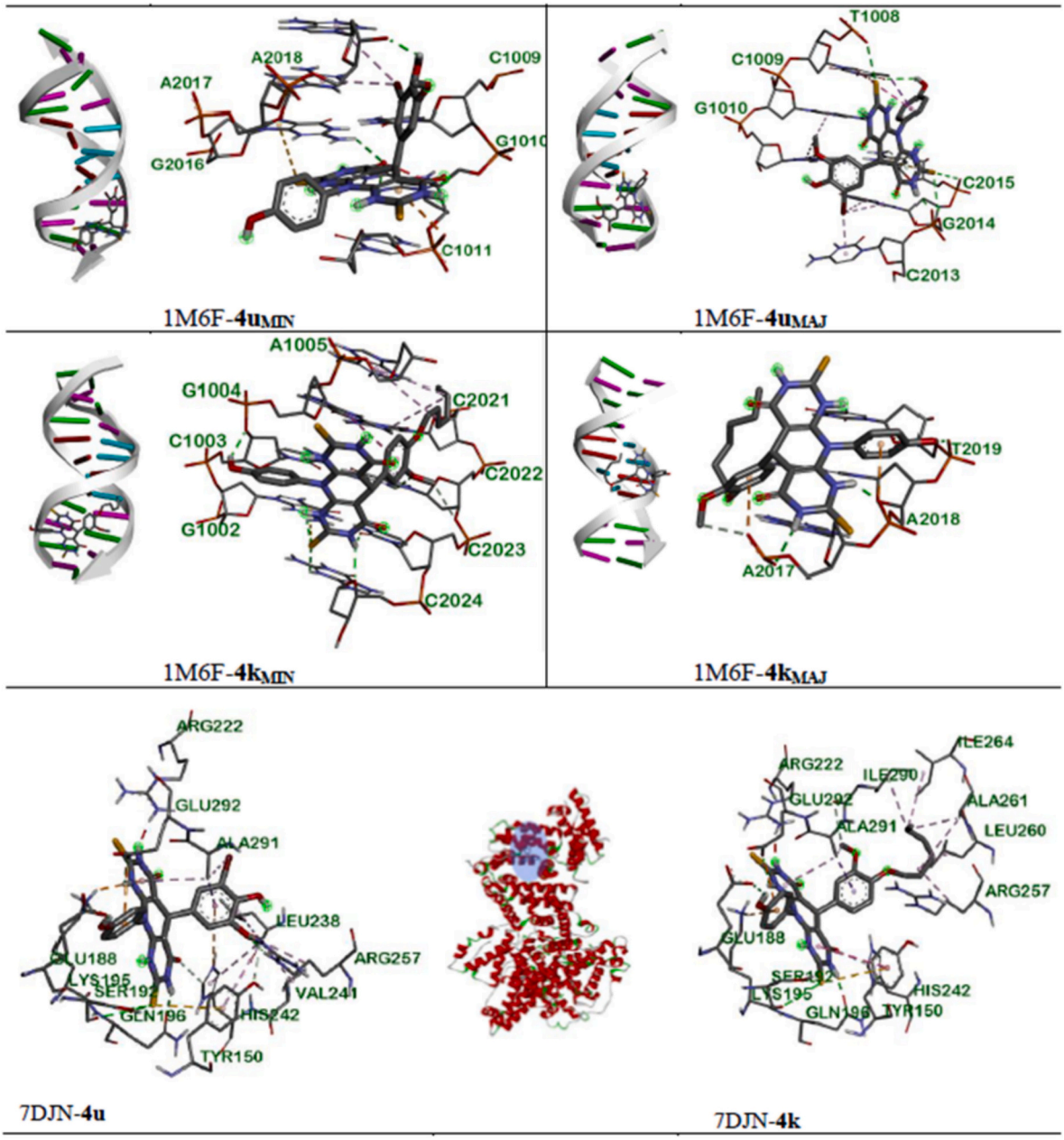

Fig. 15. Molecular docking positions of the ligands estimated in Table 8 with selected DNA and HSA molecules.

findings, RMSD and Rg profiles were analyzed for complexes involving ligands **4k** and **4u**. Both ligands, which demonstrate notable biological activity, exhibit relatively stable RMSD values throughout the simulation, reflecting preserved overall complex stability. In parallel, the Rg profiles remain well confined, indicating maintenance of protein compactness upon ligand binding. Notably, ligand **4k** shows slightly lower RMSD and less pronounced Rg fluctuations compared to **4u**, suggesting a more dynamically stable complex, which is consistent with its comparatively higher biological activity. Nevertheless, these observations are interpreted as supportive rather than deterministic, highlighting that MD-derived stability metrics complement experimental activity data without serving as direct predictors.

4. Conclusion

In this study, a new series of pyrido-dipyrimidine-based derivatives was successfully synthesized in water *via* Biginelli-like reaction and evaluated for their biological activity. The results revealed significant cytotoxic effects against HeLa and K562 cancer cell lines, while LS174 and A549 were not sensitive to the tested compounds. These findings suggest that these compounds may serve as promising candidates for the development of novel selective anticancer therapeutics Particularly, compound **4k** showed IC_{50} of 9.82 ± 1.07 μM on HeLa and SI >12 while compound 4u possess IC_{50} of 17.36 ± 1.39 μM on K562 with SI >9. Based on the potent cytotoxic activity and high selectivity observed in the MTT analysis, compounds **4k** and **4u** were selected for an in-depth investigation of their mechanism of action. Our findings demonstrate that while both compounds induce apoptosis evidenced by increased SubG1 populations and characteristic AO/EB staining they exhibit distinct execution pathways. Compound **4k** triggers caspase-3 execution *via* both intrinsic and extrinsic pathways in HeLa cells, supported by an elevation in ROS production (1.52 ± 0.15-fold). In contrast, for compound **4u** in the K562 cells, pharmacological inhibitors of caspases-3, -8, and -9 failed to attenuate the subdiploid DNA content. This observation,

Table 9
The type of interactions and corresponding interatomic distance obtained by molecular docking analysis for the most stable complex (the lowest values of ΔG_{bind} and K_i) formed between DNA (in minor and major groove) and HSA molecules and neutral forms of **4u** and **4k** ligands.

Complex	Donor – Acceptor interaction	Type of interaction	Distance (Å)
1M6F-**4u$_{MIN}$**	A: G1010: **H** - **4u**: **O**	Conventional hydrogen bond	2.65
	B: G2016: **H** - **4u**: **O**	Conventional hydrogen bond	2.92
	4u: **H** - B: A2018: **O**	Conventional hydrogen bond	2.09
	A: C1011: **O** - **4u**	π – Anion	3.85
	4u: **S** - B: G2016	π – Sulfur	5.91
	A: C1009 - **4u**: **Br**	π – Alkyl	4.70
	B: A2017 - **4u**: **Br**	π – Alkyl	4.74
	B: A2018 - **4u**: **Br**	π – Alkyl	5.27
1M6F-**4u$_{MAJ}$**	A:G1010: **H** – **4u**: **O**	Conventional hydrogen bond	1.67
	4u: **S** - A: T1008: **O**	Conventional hydrogen bond	3.19
	4u: **S** - B: G2014: **O**	Conventional hydrogen bond	3.74
	4u: **S** - B: C2015: **O**	Conventional hydrogen bond	3.38
	4u: **H** - B: G2014: **O**	Conventional hydrogen bond	1.97
	4u: **H** - A: T1008: **O**	Conventional hydrogen bond	2.60
	B: C2015: **H** - **4u**	π – Donor hydrogen bond	2.58
	A: T1008: **C** - **4u**	π – σ interactions	3.29
	4u: **S** - A: T1008	π – Sulfur	5.11
	4u: **S** - B: C2015	π – Sulfur	4.36
	A: T1008 - **4u**	π – Sulfur	5.22
	A: C1009 - **4u**: **C**	π – Alkyl	4.53
	A: G1010 - **4u**: **C**	π – Alkyl	4.73
	B: C2013 - **4u**: **Br**	π – Alkyl	3.63
	B: G2014 - **4u**: **Br**	π – Alkyl	4.54
	B: G2014 - **4u**: **Br**	π – Alkyl	5.06
1M6F-**4k$_{MIN}$**	A: G1002: **H** – **4k**: **S**	Conventional hydrogen bond	2.39
	B: G2022: **H** - **4k**: **O**	Conventional hydrogen bond	2.52
	B: G2024: **H** - **4k**: **S**	Conventional hydrogen bond	2.59
	4k: **H** - B: C2023: **O**	Conventional hydrogen bond	2.28
	4k: **H** - B: G2024: **O**	Conventional hydrogen bond	2.11
	4k: **H** - A: C1003: **O**	Conventional hydrogen bond	2.16
	4k: **C** - B: G2022: **O**	Carbon hydrogen bond	3.57
	4k: **S** - A: G1002	π – Sulfur	5.42
	A: G1004 - **4k**	π – Sulfur	5.72
	A: A1005 - **4k**	π – Alkyl	5.05
	A: A1005 - **4k**: **C**	π – Alkyl	5.08
	B: C2021 - **4k**: **C**	π – Alkyl	5.40
1M6F-**4k$_{MAJ}$**	**4k**: **H** - B: A2017: **O**	Conventional hydrogen bond	2.28
	4k: **H** - B: A2018: **O**	Conventional hydrogen bond	1.89
	4k: **H** - B: T2019: **O**	Conventional hydrogen bond	2.20
	4k: **C** - B: A2017: **O**	Carbon hydrogen bond	3.13
	B: A2017: **O** - **4k**	π – Anion	3.65
	B: A2018: **O** - **4k**:	π – Anion	2.93
7DJN-**4u**	Arg257: **H** - **4u**: **O**	Conventional hydrogen bond	2.05
	4u: **S** - Ser192: **O**	Conventional hydrogen bond	3.35
	4u: **S** - Ser192: **O**	Conventional hydrogen bond	2.57
	4u: **H** - Glu292: **O**	Conventional hydrogen bond	2.07
	4u: **H** - Gln196: **O**	Conventional hydrogen bond	2.07
	4u: **H** - Glu188: **O**	Conventional hydrogen bond	2.35
	His242: **C** - **4u**: **O**	Carbon hydrogen bond	2.67
	4u: **C** - Tyr150: **O**	Carbon hydrogen bond	2.60
	Lys195: **H** - **4u**	π – Cation; π – Donor hydrogen bond	2.85
	Lys195: **H** - **4u**	π – Cation; π – Donor hydrogen bond	2.88
	His242: **N** - **4u**	π – Cation	4.90
	Glu292: **O** - **4u**	π – Anion	3.78
	Ala291: **C** - **4u**	π – σ interactions	3.41
	4u: **S** - Tyr150	π – Sulfur	4.60
	Ala291 - **4u**: **Br**	Alkyl	4.27
	4u: **C** - Leu238	Alkyl	5.49
	4u: **C** - Val241	Alkyl	4.76
	4u: **C** - Arg257	Alkyl	3.90
	Tyr150 - **4u**: **C**	π – Alkyl	4.94
	His242 - **4u**: **C**	π – Alkyl	5.05
	4u - Ala291	π – Alkyl	4.24
7DJN-**4k**	**4k**: **S** - Ser192: **O**	Conventional hydrogen bond	2.99
	4k: **S** - Ser192: **O**	Conventional hydrogen bond	2.59
	4k: **H** - Glu292: **O**	Conventional hydrogen bond	2.22
	4k: **H** - Gln196: **O**	Conventional hydrogen bond	1.79
	4k: **H** - Glu188: **O**	Conventional hydrogen bond	2.47
	His242: **C** - **4k**: **O**	Carbon hydrogen bond	2.62
	4k: **C** - Ile290: **O**	Carbon hydrogen bond	3.63
	Lys195: **H** - **4k**	π – Cation; π – Donor hydrogen bond	2.85
	Glu292: **O** - **4k**	π – Anion	3.84
	Ala291: **C** - **4k**	π – σ interactions	3.58
	4k: **S** - Tyr150	π – Sulfur	4.81
	Tyr150 - **4k**	π – π stacked	4.84
	Arg257 - **4k**	Alkyl	3.83
	Ala261 - **4k**	Alkyl	4.63
	Ala261 - **4k**: **C**	Alkyl	4.10
	Ala291 - **4k**: **C**	Alkyl	4.29
	4k - Leu260	Alkyl	4.59
	4k: **C** - Ile264	Alkyl	5.00
	4k: **C** - Ile290	Alkyl	3.79
	4k - Ala291	π – Alkyl	4.29

coupled with a discreet but consistent 1.07 ± 0.08-fold elevation in ROS levels, indicates that the apoptotic response induced by **4u** in K562 cells proceeds regardless of caspase activity. This divergence in apoptotic mode is rationally attributed to structural variations at the R2 and R3 positions. The flexible, lipophilic hexyloxy substituent in **4k** likely favors interactions that engage the classical caspase cascade. In contrast, the more compact, halogen-substituted and electronically polarized structure of **4u** appears to facilitate a bypass of the caspase machinery, potentially shifting the trigger toward ROS mediated signaling. Furthermore, the binding modes to key biomacromolecules, such as DNA and HSA, were explored *in silico* and confirmed using absorption and fluorescence techniques. Although the present research was limited to *in vitro* evaluation, these findings provide a strong rationale for further *in vivo* investigations and systematic structural optimization. Overall, this work offers valuable insights into how small structural modifications within the same scaffold can modulate the biochemical route of cell death, contributing to the ongoing efforts in targeted cancer drug discovery.

CRediT authorship contribution statement

Lazar Milović: Methodology, Investigation, Formal analysis. **Nađa Grozdanić:** Methodology, Investigation, Formal analysis. **Tatjana Stanojković:** Methodology, Investigation. **Jelena Đorović Jovanović:**

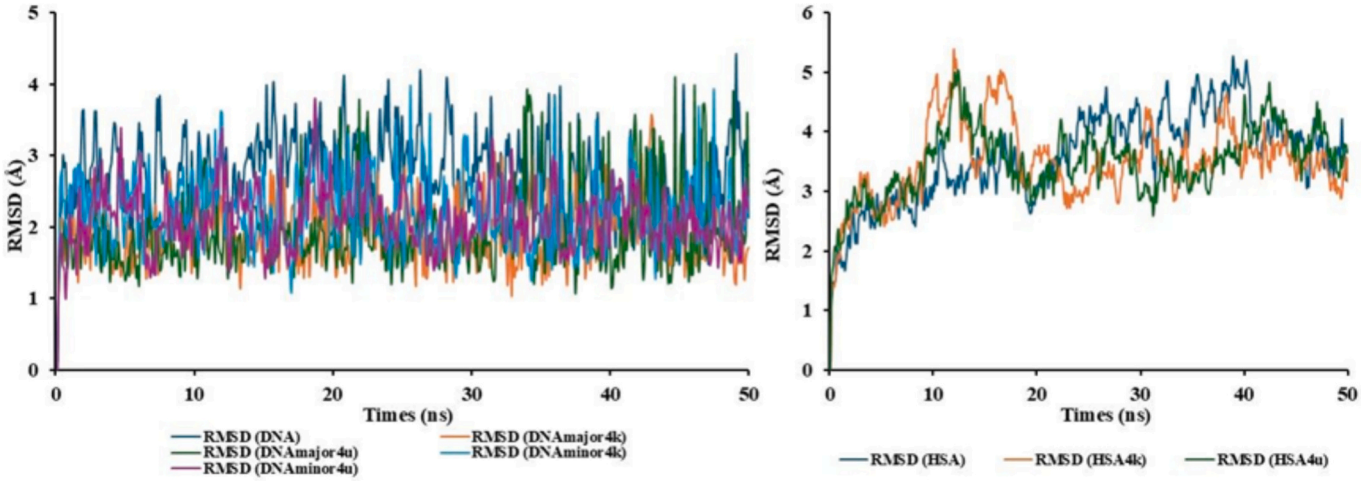

Fig. 16. RMSD diagram describing the changes in protein-ligand complexes after binding **4k** and **4u** to DNA and HSA.

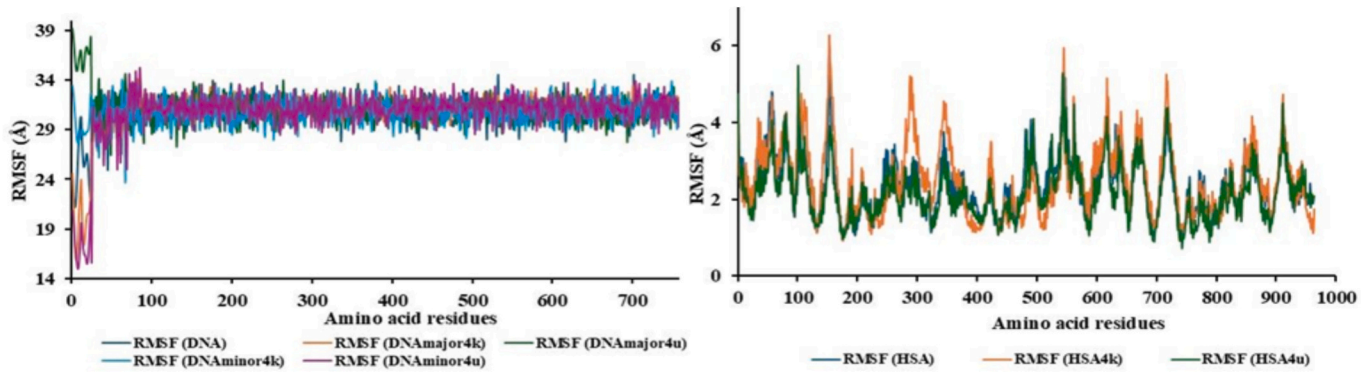

Fig. 17. RMSF diagram describing the changes in protein-ligand complex after binding **4k** and **4u** to DNA and HAS.

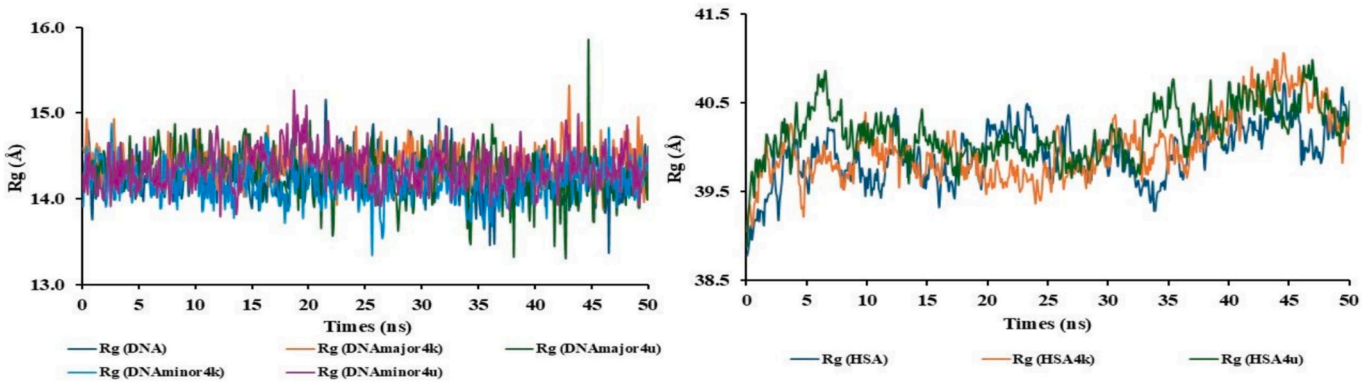

Fig. 18. Rg diagram describing the changes in protein-ligand complexes after binding **4k** and **4u** to DNA and HSA.

Methodology, Investigation. **Svetlana Jeremić:** Methodology, Investigation. **Maja Petrović:** Methodology, Investigation. **Milica Marković:** Methodology, Investigation. **Ana Rilak Simović:** Methodology, Investigation. **Nenad Janković:** Writing – original draft, Supervision, Conceptualization.

Declaration of competing interest

The authors declare that they have no known competing financial interests or personal relationships that could have appeared to influence the work reported in this paper.

Acknowledgment

This research has been supported by the Ministry of Science, Technological Development and Innovation [Contract No. 451-03-33/2026-03/200378, 451-03-33/2026-03/200043 and (SR)0260206)].

Appendix A. Supplementary data

Supplementary data to this article can be found online at https://doi.org/10.1016/j.bioorg.2026.109740.

Data availability

Data will be made available on request.

References

[1] B.B. Thompson, J. Montgomery, Enone-alkyne reductive coupling: a versatile entry to substituted pyrroles, Org. Lett. 13 (2011) 3289–3291, https://doi.org/10.1021/ol201133n.

[2] B.S. Vachan, M. Karuppasamy, P. Vinoth, S. Vivek Kumar, S. Perumal, V. Sridharan, J.C. Menendez, Proline and its derivatives as organocatalysts for multi-component reactions in aqueous media: synergic pathways to the green synthesis of heterocycles, Adv. Synth. Catal. 362 (2020) 87–110, https://doi.org/10.1002/adsc.201900558.

[3] T. Suresh, P.S. Mohan, Synthesis and antibacterial activities of 1,2,3,4,6,7,8,9-octahydro-1,3,7,9-tetraphenyl 5-pyrrolo-2,4,6,8-tetraoxo-10H,5H-pyrido[2,3-d;6,5-d']dipyrimidine, Heterocycl. Commun. 9 (2003) 203–208, https://doi.org/10.1515/HC.2003.9.2.203.

[4] M. Dabiri, H. Arvin-Nezhad, H.R. Khavasi, A. Bazgir, A novel and efficient synthesis of pyrimido[4,5-d]pyrimidine-2,4,7-trione and pyrido[2,3-d:6,5-d]dipyrimidine-2,4,6,8-tetrone derivatives, Tetrahedron 63 (2007) 1770–1774, https://doi.org/10.1016/j.tet.2006.12.043.

[5] S. Rostamizadeh, L. Tahershamsi, N. Zekri, An efficient, one-pot synthesis of pyrido[2,3-d:6,5-d']dipyrimidines using SBA-15-supported sulfonic acid nanocatalyst under solvent-free conditions, J. Iran. Chem. Soc. 12 (2015) 1381–1389, https://doi.org/10.1007/s13738-015-0604-1.

[6] Z. Lin, H. Hu, X. You, X. Zhang, Y. Gao, An efficient synthesis of pyrido[2,3-d:6,5-d]dipyrimidine and 5,5′-arylmethylenebis(2,6-diaminopyrimidinone) derivatives under microwave irradiation, J. Heterocyclic Chem. 51 (2014) 277–283, https://doi.org/10.1002/jhet.1647.

[7] L. Cordeu, E. Cubedo, E. Bandrés, A. Rebollo, X. Sáenz, H. Chozas, M. V. Domínguez, M. Echeverri, B. Mendivil, C. Sanmartin, J.A. Palop, M. Fontc, J. García-Foncillas, Biological profile of new apoptotic agents based on 2,4-pyrido[2,3-d]pyrimidine derivatives, Bioorg. Med. Chem. 15 (2007) 1659–1669, https://doi.org/10.1016/j.bmc.2006.12.010.

[8] A.E. Rashad, H.H. Sayed, A.H. Shamroukh, H.M. Awad, Preparation of some fused pyridopyrimidine and pyridothienotriazine derivatives for biological evaluation, Phosphorus Sulfur Silicon Relat. Elem. 180 (2005) 2767–2777, https://doi.org/10.1080/104265090968118.

[9] J. Quiroga, P.E. Romo, A. Ortiz, J.H. Isaza, B. Insuasty, R. Abonia, M. Nogueras, J. Cobo, Synthesis, structures, electrochemical studies and antioxidant activity of 5-aryl-4-oxo-3,4,5,8-tetrahydropyrido[2,3-d]pyrimidine-7-carboxylic acids, J. Mol. Struct. 1120 (2016) 294–301, https://doi.org/10.1016/j.molstruc.2016.05.045.

[10] L.N. Bheemanapalli, R.R. Akkinepally, S.R. Pamulaparthy, Synthesis and antibacterial activity of a new series of 2,3,5,7-substituted-pyrido[2,3-d]pyrimidin-4(3H)-one derivatives, Chem. Pharm. Bull. 56 (2008) 1342–1348, https://doi.org/10.1248/cpb.56.1342.

[11] H. Huang, D.A. Hutta, H. Hu, R.L. DesJarlais, C. Schubert, I.P. Petrounia, M. A. Chaikin, C.L. Manthey, M.R. Player, Design and synthesis of a pyrido[2,3-d]pyrimidin-5-one class of anti-inflammatory FMS inhibitors, Bioorg. Med. Chem. Lett. 18 (2008) 2355–2361, https://doi.org/10.1016/j.bmcl.2008.02.070.

[12] M.M. Gineinah, M.N.A. Nasr, S.M.I. Badr, Synthesis and antitumor activity of new pyrido[2,3-d]pyrimidine derivatives, Med. Chem. Res. 22 (2013) 3943–3952, https://doi.org/10.1007/s00044-012-0396-0.

[13] H. Naeimi, A. Didar, Z. Rashid, Z. Zahraie, Sonochemical synthesis of pyrido[2,3-d:6,5-d']dipyrimidines catalyzed by [HNMP]+[HSO4]− and their antimicrobial activity studies, J. Antibiot. 70 (2017) 845–852, doi:1038/10./ja.2017.47.

[14] H.N. Hafez, A.R.B. El-Gazzar, A.S. Ali, A.A.I. Alakhras, Design, synthesis, and biological evaluation of n-phenylpyrazole derivatives featuring nitrogen-containing side chains as potent antitumor agents, Egypt. J. Chem. 62 (2019) 1093–1104, https://doi.org/10.21608/ejchem.2019.6773. 1565.

[15] A.R.B. El-Gazzar, H.N. Hafez, Synthesis of 4-substituted pyrido[2,3-d]pyrimidin-4(1H)-one as analgesic and anti-inflammatory agents, Bioorg. Med. Chem. Lett. 19 (2009) 3392–3397.

[16] K. Akagi, M. Hirose, T. Hoshiya, Y. Mizoguchi, N. Ito, T. Shirai, Modulating effects of ellagic acid, vanillin and quercetin in a rat medium-term multi-organ carcinogenesis model, Cancer Lett. 94 (1995) 113–121.

[17] M.M. Shaikh, M.A.K. Azad, M. Jesmin, S. Ahsan, M.M. Rahman, J.A. Khanam, M. N. Islam, S.M.S. Shahriar, In vivo anticancer activity of vanillin semicarbazone, Asian Pac. J. Trop. Biomed. 2 (2012) 438–442, https://doi.org/10.1016/S2221-1691(12)60072-0.

[18] L. Blaikie, G. Kay, P.K.T. Lin, Synthesis and in vitro evaluation of vanillin derivatives as multi-target therapeutics for the treatment of Alzheimer's disease, Bioorg. Med. Chem. Lett. 30 (2020) 127505, https://doi.org/10.1016/j.bmcl.2020.127505.

[19] A. Tai, T. Sawano, F. Yazama, Antioxidant properties of ethyl vanillin in vitro and in vivo, Biosci. Biotechnol. Biochem. 75 (2011) 2346–2350, https://doi.org/10.1271/bbb.110524.

[20] C.S.N.R. Teixeira, I.M.D. Martins, V.L.G. Mata, M.F. Filipe Barreiro, A.E. Rodrigues, J. Text. Inst. 103 (2011) 269.

[21] F. Kayaci, T. Uyar, Encapsulation of vanillin/cyclodextrin inclusion complex in electrospun polyvinyl alcohol (PVA) nanowebs: Prolonged shelf-life and high temperature stability of vanillin, Food Chem 133 (2012) 641, https://doi.org/10.1016/j.foodchem.2012.01.040.

[22] F. Kayaci, T. Uyar, Solid Inclusion Complexes of Vanillin with Cyclodextrins: Their Formation, Characterization, and High-Temperature Stability, J. Agric. Food Chem. 59 (2011) 11772, https://doi.org/10.1021/jf202915c.

[23] S.S. Chobe, B.S. Dawane, K.M. Tumbi, P.P. Nandekar, A.T. Sangamwar, An ecofriendly synthesis and DNA binding interaction study of some pyrazolo[1,5-a]pyrimidine derivatives, Bioorg. Med. Chem. Lett. 22 (2012) 7566–7572.

[24] Refn, Shankaraiah, C. Jadala, S. Nekkanti, K.R. Senwar, N. Nagesh, S. Shrivastava, V.G.M. Naidu, V. Sathish, A. Kamal, Design and synthesis of C3-tethered 1,2,3-triazolo-β-carboline derivatives: anticancer activity, DNA-binding ability, viscosity and molecular modeling studies, Bioorg. Chem. 64 (2016) 42–50.

[25] A. Gaber, A. Abo Elmaaty, M. Sharaky, A.A. Mosa, A.Y.A. Alzahrani, S. Shaaban, W. M. Eldehna, A.A. Al-Karmalawy, Multi-target rational design and synthesis of novel diphenyl-tethered pyrazolopyrimidines targeting EGFR and topoisomerase II with potential DNA intercalation and apoptosis induction, Bioorg. Chem. 145 (2024) 107223, https://doi.org/10.1016/j.bioorg.2024.107223.

[26] P. Pinar, P. Yurdakul, I. Yildiz, O. Temiz-Arpaci, N.L. Acan, E. Aki-Sener, I. Yalcin, Some fused heterocyclic compounds as eukaryotic topoisomerase II inhibitors, Biochem. Biophys. Res. Commun. 317 (2004) 670–674, https://doi.org/10.1016/j.bbrc.2004.03.093.

[27] P.A. Yakkala, N.R. Penumallu, S. Shafi, A. Kamal, Prospects of topoisomerase inhibitors as promising anti-cancer agents, Pharmaceuticals (Basel) 16 (2023) 1456, https://doi.org/10.3390/ph16101456.

[28] T. Mosmann, Rapid colorimetric assay for cellular growth and survival: application to proliferation and cytotoxicity assays, J. Immunol. Methods 65 (1983) 55–63, https://doi.org/10.1016/0022-1759(83)90303-4.

[29] M. Ohno, T. Abe, Rapid colorimetric assay for the quantification of leukemia inhibitory factor (LIF) and interleukin-6 (IL-6), J. Immunol. Methods 145 (1991) 199–203, https://doi.org/10.1016/0022-1759(91)90327-C.

[30] I.Z. Matić, I. Aljančić, Ž. Žižak, V. Vajs, M. Jadranin, S. Milosavljević, Z.D. Juranić, In vitro antitumor actions of extracts from endemic plant Helichrysum zivojinii, BMC Complement. Altern. Med. 13 (2013) 36, doi: 10.1186/1472-6882-13-36.

[31] B. Nguyen, M.P.H. Lee, D. Hamelberg, A. Joubert, C. Bailly, R. Brun, S. Neidle, W. D. Wilson, Strong binding in the DNA minor groove by an aromatic diamidine with a shape that does not match the curvature of the groove, J. Am. Chem. Soc. 124 (2002) 13680–13681, https://doi.org/10.1021/ja027953c.

[32] H. Berman, K. Henrick, H. Nakamura, Announcing the worldwide protein data Bank, Nat. Struct. Mol. Biol. 10 (2003) 980, https://doi.org/10.1038/nsb1203-980.

[33] BIOVIA DS, Discovery Studio Modeling Environment, BIOVIA, San Diego, 2025.

[34] G.M. Morris, R. Huey, W. Lindstrom, et al., AutoDock4 and AutoDockTools4: automated docking with selective receptor flexibility, J. Comput. Chem. 30 (2009) 2785–2791, https://doi.org/10.1002/jcc.21256.

[35] M.S. Valdés-Tresanco, M.E. Valdés-Tresanco, P.A. Valiente, et al., AMDock: a versatile graphical tool for assisting molecular docking with AutoDock Vina and AutoDock4, Biol. Direct 15 (2020) 12, https://doi.org/10.1186/s13062-020-00267-2.

[36] Y. Zhang, S. Forli, A. Omelchenko, M.F. Sanner, AutoGridFR: improvements on AutoDock affinity maps and associated software tools, J. Comput. Chem. 40 (2019) 2882–2886, https://doi.org/10.1002/jcc.26054.

[37] G.M. Morris, D.S. Goodsell, R.S. Halliday, R. Huey, W.E. Hart, R.K. Belew, A. J. Olson, Automated docking using a Lamarckian genetic algorithm and an empirical binding free energy function, J. Comput. Chem. 19 (1998) 1639–1662, https://doi.org/10.1002/(SICI)1096-987X(19981115)19:14.

[38] M.J. Frisch, G.W. Trucks, H.B. Schlegel, G.E. Scuseria, M.A. Robb, J.R. Cheeseman, et al., *Gaussian 09*, Revision A.02, Gaussian, Inc., Wallingford CT, 2009.

[39] Playground v1.6.2, **Accessed November**, https://playground.calculators.cxn.io/, **2024**.

[40] D.A. Case, H.M. Aktulga, K. Belfon, I.Y. Ben-Shalom, J.T. Berryman, S.R. Brozell, et al., Amber 2024, University of California, San Francisco, 2024.

[41] D.A. Case, H.M. Aktulga, K. Belfon, D.S. Cerutti, G.A. Cisneros, V.W.D. Cruzeiro, et al., AmberTools, J. Chem. Inf. Model. 63 (2023) 6183–6191.

[42] D.J. Price, C.L. Brooks III, A modified TIP3P water potential for simulation with Ewald summation, J. Chem. Phys. 121 (2004) 10096–10103, https://doi.org/10.1063/1.1808117.

[43] K.G. Sprenger, V.W. Jaeger, J. Pfaendtner, The general AMBER force field (GAFF) can accurately predict thermodynamic and transport properties of many ionic liquids, J. Phys. Chem. B 119 (2015) 5882–5895, https://doi.org/10.1021/acs.jpcb.5b00689.

[44] J.A. Maier, C. Martinez, K. Kasavajhala, L. Wickstrom, K.E. Hauser, C. Simmerling, ff14SB: improving the accuracy of protein side chain and backbone parameters from ff99SB, J. Chem. Theory Comput. 11 (2015) 3696–3713, https://doi.org/10.1021/acs.jctc.5b00255.

[45] J. Wang, R.M. Wolf, J.W. Caldwell, P.A. Kollman, D.A. Case, Development and testing of a general AMBER force field, J. Comput. Chem. 25 (2004) 1157–1174, https://doi.org/10.1002/jcc.20035.

[46] U. Essmann, L. Perera, M.L. Berkowitz, T. Darden, H. Lee, L.G. Pedersen, A smooth particle mesh Ewald method, J. Chem. Phys. 103 (1995) 8577–8593, https://doi.org/10.1063/1.470117.

[47] N. Shahabadi, S. Hadidi, Spectroscopic studies on the interaction of calf thymus DNA with the drug levetiracetam, Spectrochim. Acta A Mol. Biomol. Spectrosc. 96 (2012) 278–283, https://doi.org/10.1016/j.saa.2012.05.045.